Research Square

Preprints are preliminary reports that have not undergone peer review.
They should not be considered conclusive, used to inform clinical practice,
or referenced by the media as validated information.

Probabilistic Modeling of Spacecraft Venting Disturbances for Crewed Missions

Andrea Rigato

andrea.rigato@utexas.edu

The University of Texas at Austin

Felipe Giraldo-Grueso

NASA Johnson Space Center (JETS II–Amentum)

Christopher D'Souza

NASA Johnson Space Center

Jack Joshi

The University of Texas at Austin

Matthew Gualdoni

NASA Johnson Space Center

Renato Zanetti

The University of Texas at Austin

Research Article

Keywords: Spacecraft venting, point processes, navigation filtering, attitude uncertainty, crewed spacecraft

Posted Date: November 13th, 2026

DOI: https://doi.org/10.21203/rs.3.rs-11252883/v1

License: This work is licensed under a Creative Commons Attribution 4.0 International License.
Read Full License

Additional Declarations: No competing interests reported.

Probabilistic Modeling of Spacecraft Venting Disturbances for Crewed Missions

Andrea Rigato[1*], Felipe Giraldo-Grueso[2], Christopher D'Souza[3], Jack Joshi[1], Matthew Gualdoni[3], Renato Zanetti[1]

[1*]Department of Aerospace Engineering and Engineering Mechanics, The University of Texas at Austin, Austin, 78712, TX, United States.
[2]NASA Johnson Space Center (JETS II–Amentum), Houston, 77058, TX, United States.
[3]NASA Johnson Space Center, Houston, 77058, TX, United States.

*Corresponding author(s). E-mail(s): andrea.rigato@utexas.edu;
Contributing authors: felipe.giraldogrueso@nasa.gov; chris.dsouza-1@nasa.gov; jack.a.joshi@my.utexas.edu; matthew.j.gualdoni@nasa.gov; renato@utexas.edu;

Abstract

Spacecraft venting produces small, cumulative trajectory disturbances that can degrade navigation accuracy during crewed missions. Accurately representing these disturbances in a navigation filter requires accounting for uncertainty in the event timing, impulse magnitude, and inertial direction. This paper models venting disturbances as a marked Gaussian–Poisson point process: the number of events follows a Poisson distribution, the impulse magnitudes are Gaussian distributed, and the vent direction is characterized by its first two moments. Closed-form expressions are derived for the mean disturbance and the associated process noise covariance. The model is evaluated through Monte Carlo simulations of a spacecraft in a near-rectilinear halo orbit, including instantaneous and finite-duration vent profiles and several models of directional uncertainty. The predicted covariance closely agrees with the empirical state dispersion across the numerous cases considered, supporting the use of the proposed formulation in navigation filters for crewed missions.

Keywords: Spacecraft venting, point processes, navigation filtering, attitude uncertainty, crewed spacecraft

1 Introduction

Crewed exploration missions beyond low Earth orbit, particularly those returning to the lunar vicinity with the Artemis program, demand precise navigation and control to ensure crew safety and mission success. The Orion spacecraft, serving as the primary crew vehicle for these expeditions, relies on its Environmental Control and Life Support System (ECLSS) to maintain habitable conditions. This includes periodic venting operations to expel carbon dioxide, excess humidity, waste water, and other byproducts. While essential for crew health, these venting events impart small but non-negligible disturbances to the vehicle's trajectory. Over the course of multi-day transits, the cumulative effect of such perturbations can degrade navigation performance, increase trajectory dispersions, and complicate guidance, navigation, and control functions both onboard and on the ground. Specifically, the new formulation presented here is motivated by the venting perturbations that will be experienced during the Artemis missions. However, these and other perturbations, such as cryogenic venting, are anticipated to occur in future crewed missions as well.

During the Apollo missions, urine (or waste water (WW)) vents were specifically scheduled before trajectory correction burns to minimize the resulting trajectory dispersions [1, 2]. These vents were also designed to prevent saturation of the field of view during key measurement periods. In addition to WW vents, the crewed Artemis missions will also have ammonia boiler and pressure swing adsorption (PSA) vents. The PSA vents will be responsible for removing CO_2 and humidity. Neither of these vents existed during the Apollo missions and, in place of the PSA vents, CO_2 was absorbed onboard using lithium hydroxide canisters [3]. The PSA vents for Artemis II are expected to have a much greater impact on trajectory dispersions than the WW vents, which already had a noticeable impact during the Apollo era. Therefore, correctly characterizing the effect of each vent on the trajectory is important to ensure crew safety.

To accurately capture the effects of venting on trajectory dispersions, the vents must be carefully modeled, as both onboard and ground-based navigation systems may have difficulty measuring the resulting accelerations. The onboard navigation is unable to capture the venting effects as they are below the detectable threshold of the onboard inertial sensors. While ground observation systems may be able to track the accelerations caused by these vents, they are limited in characterizing their effects if the vent directions are unobservable to the sensors. Therefore, the vents must be accurately modeled to be included in the navigation solutions. To model the perturbations correctly, three sources of randomness must be accounted for. The first is the magnitude of each vent, which can be modeled to be Gaussian distributed with some non-zero mean and an associated variance. The second is the time of arrival of each vent. Even though the vents can be scheduled, their time of arrival is still inherently uncertain. The third source of randomness is the vent direction. Even when the vent direction is known with high accuracy in the spacecraft body frame, uncertainty in the spacecraft attitude introduces uncertainty in the corresponding direction expressed in the inertial frame.

Previous approaches have modeled these perturbations by assuming that the vent magnitudes are random, but the vent schedule and direction are perfectly known. For

instance, under these assumptions, the acceleration perturbations caused by the vents can be modeled as zero-mean first-order Markov processes [4]. To account for the non-zero mean nature of the vents, the associated covariance can be artificially inflated. However, to better capture the effect of the non-zero mean vents, a perturbed nominal approach has also been introduced [5]. In both of these proposed approaches, only the randomness in the vent magnitudes has been considered, and it has been assumed that the timing and direction of each vent were known and fixed. As mentioned earlier, the actual vent timings and directions are unknown beforehand and must be treated as random processes within the filter. In practice, vent perturbations have been incorporated into the filter by tuning a process noise covariance to match results obtained from Monte Carlo (MC) analysis.

To account for these three sources of uncertainty, this paper introduces a Gaussian–Poisson point-process model for venting perturbations. Within this framework, the number of venting events occurring over a given time interval is modeled as a Poisson random variable, the vent magnitudes are modeled as Gaussian random variables, and the vent direction is characterized through its first and second moments. This formulation allows both the magnitude and direction of each vent to be uncertain while accounting for the stochastic arrival times of the events. The Poisson distribution is used to model the number of vents, as the vents are assumed to be independent of one another. This new approach is used to derive an associated process noise covariance, which can better reflect the navigation perturbations associated with the venting.

The remainder of this paper is organized as follows. Section 2 presents preliminaries on nonlinear state dynamics and linearized error dynamics. Section 3 defines the spacecraft translational dynamics considered in this paper and introduces the proposed point-process approach. Section 4 derives the error and covariance propagation equations used for filtering. The proposed approach is then evaluated against MC results for different venting scenarios in section 5. Finally, section 6 presents the concluding remarks, highlighting the relevance of the proposed venting model for future human spaceflight missions. A comparison between the proposed point-process approach and the filter-tuning strategies currently used in practice is provided in the appendix.

2 Preliminaries

This section reviews the linearization of nonlinear dynamics about a nominal trajectory and the corresponding solution of the linearized error dynamics. These results are used throughout the subsequent development.

Consider the nonlinear dynamical system

$$\dot{\boldsymbol{x}}(t) = \boldsymbol{f}(\boldsymbol{x}(t), \boldsymbol{u}(t), t)\,, \tag{1}$$

where $\boldsymbol{x} \in \mathbb{R}^n$ is the state vector and $\boldsymbol{u} \in \mathbb{R}^m$ is the input vector. Let $\bar{\boldsymbol{x}}(t)$ and $\bar{\boldsymbol{u}}(t)$ denote a nominal trajectory satisfying

$$\dot{\bar{\boldsymbol{x}}}(t) = \boldsymbol{f}(\bar{\boldsymbol{x}}(t), \bar{\boldsymbol{u}}(t), t)\,. \tag{2}$$

The state and input perturbations are defined as

$$\delta \boldsymbol{x}(t) = \boldsymbol{x}(t) - \bar{\boldsymbol{x}}(t), \tag{3}$$

$$\delta \boldsymbol{u}(t) = \boldsymbol{u}(t) - \bar{\boldsymbol{u}}(t). \tag{4}$$

A first-order Taylor series expansion of $\boldsymbol{f}$ about the nominal trajectory yields the linearized dynamics

$$\delta \dot{\boldsymbol{x}}(t) = \boldsymbol{A}(t)\, \delta \boldsymbol{x}(t) + \boldsymbol{B}(t)\, \delta \boldsymbol{u}(t), \tag{5}$$

where

$$\boldsymbol{A}(t) = \left.\frac{\partial \boldsymbol{f}}{\partial \boldsymbol{x}}\right|_{\bar{\boldsymbol{x}},\bar{\boldsymbol{u}}}, \qquad \boldsymbol{B}(t) = \left.\frac{\partial \boldsymbol{f}}{\partial \boldsymbol{u}}\right|_{\bar{\boldsymbol{x}},\bar{\boldsymbol{u}}}. \tag{6}$$

The matrix $\boldsymbol{A}(t)$ is the state Jacobian, and $\boldsymbol{B}(t)$ characterizes the sensitivity of the dynamics to input perturbations.

The solution of eq. (5) can be expressed in terms of the state transition matrix (STM), $\boldsymbol{\Phi}(t, t_0)$, which satisfies [6]

$$\begin{cases} \dot{\boldsymbol{\Phi}}(t, t_0) = \boldsymbol{A}(t)\boldsymbol{\Phi}(t, t_0), \\ \boldsymbol{\Phi}(t_0, t_0) = \boldsymbol{I}_n, \end{cases} \tag{7}$$

where $\boldsymbol{I}_n$ is the $n \times n$ identity matrix. The perturbation state at time t is then given by

$$\delta \boldsymbol{x}(t) = \boldsymbol{\Phi}(t, t_0)\, \delta \boldsymbol{x}(t_0) + \int_{t_0}^{t} \boldsymbol{\Phi}(t, \tau)\boldsymbol{B}(\tau)\delta \boldsymbol{u}(\tau)\, d\tau. \tag{8}$$

The first term propagates the initial state perturbation through the system dynamics, whereas the second term captures the effect of the input perturbation.

For general nonlinear systems, the state transition matrix is obtained by integrating eq. (7). When the system Jacobian varies slowly over a sufficiently short interval $\Delta t = t - t_0$, however, $\boldsymbol{A}(t)$ may be approximated as constant

$$\boldsymbol{A}(t) \approx \boldsymbol{A}(t_0) = \boldsymbol{A}_0. \tag{9}$$

In this case, the state transition matrix is approximated by

$$\boldsymbol{\Phi}(t, t_0) \approx \exp(\boldsymbol{A}_0 \Delta t)\,. \tag{10}$$

For a short propagation interval, the matrix exponential can then be approximated by its Taylor series:

$$\boldsymbol{\Phi}(t, t_0) \approx \boldsymbol{I}_n + \boldsymbol{A}_0 \Delta t + \frac{1}{2}\boldsymbol{A}_0^2 \Delta t^2 + \frac{1}{6}\boldsymbol{A}_0^3 \Delta t^3 + \cdots. \tag{11}$$

Alternatively, the same approximation can be obtained from the Peano–Baker series by assuming that the system matrix $\boldsymbol{A}(t)$ is constant over the propagation interval.

Under this assumption, the Peano–Baker series reduces to the Taylor expansion in eq. (11) [7].

3 Venting Disturbance Model

This section introduces the spacecraft translational dynamics and develops the stochastic model used to characterize venting disturbances.

Consider the translational dynamics of a spacecraft

$$\begin{aligned} \dot{\boldsymbol{r}}(t) &= \boldsymbol{v}(t), \\ \dot{\boldsymbol{v}}(t) &= \boldsymbol{g}(\boldsymbol{r}(t)) + \boldsymbol{a}_v(t), \end{aligned} \tag{12}$$

where $\boldsymbol{r} \in \mathbb{R}^3$ and $\boldsymbol{v} \in \mathbb{R}^3$ are the spacecraft position and velocity expressed in an inertial reference frame. The function $\boldsymbol{g}(\cdot) : \mathbb{R}^3 \to \mathbb{R}^3$ represents the gravitational acceleration, and $\boldsymbol{a}_v$ is the acceleration induced by venting disturbances.

The dynamics in eq. (12) are not intended as a high-fidelity model of the complete spacecraft environment. Additional perturbations, such as atmospheric drag, and solar-radiation pressure, may be required in an operational model [8]. The simplified dynamics are nevertheless sufficient to isolate the stochastic properties of venting disturbances and their effect on spacecraft motion.

Let the nominal trajectory be defined by $\bar{\boldsymbol{r}}(t)$, $\bar{\boldsymbol{v}}(t)$, and $\bar{\boldsymbol{a}}_v(t)$, satisfying

$$\begin{aligned} \dot{\bar{\boldsymbol{r}}}(t) &= \bar{\boldsymbol{v}}(t), \\ \dot{\bar{\boldsymbol{v}}}(t) &= \boldsymbol{g}(\bar{\boldsymbol{r}}(t)) + \bar{\boldsymbol{a}}_v(t). \end{aligned} \tag{13}$$

Defining the perturbations $\delta\boldsymbol{r} = \boldsymbol{r} - \bar{\boldsymbol{r}}$, $\delta\boldsymbol{v} = \boldsymbol{v} - \bar{\boldsymbol{v}}$, $\delta\boldsymbol{a}_v = \boldsymbol{a}_v - \bar{\boldsymbol{a}}_v$, and then linearizing the dynamics about the nominal trajectory, gives

$$\begin{aligned} \delta\dot{\boldsymbol{r}}(t) &= \delta\boldsymbol{v}(t), \\ \delta\dot{\boldsymbol{v}}(t) &= \boldsymbol{G}(\bar{\boldsymbol{r}}(t))\,\delta\boldsymbol{r}(t) + \delta\boldsymbol{a}_v(t), \end{aligned} \tag{14}$$

where $\boldsymbol{G}(\cdot)$ is the Jacobian of the gravitational acceleration

$$\boldsymbol{G}(\bar{\boldsymbol{r}}(t)) = \left.\frac{\partial \boldsymbol{g}}{\partial \boldsymbol{r}}\right|_{\bar{\boldsymbol{r}}}. \tag{15}$$

The error dynamics can be rewritten in state-space form as

$$\delta\dot{\boldsymbol{x}}(t) = \boldsymbol{A}(t)\,\delta\boldsymbol{x}(t) + \boldsymbol{B}\,\delta\boldsymbol{a}_v(t) \tag{16}$$

where $\boldsymbol{x} = \begin{bmatrix}\boldsymbol{r}^T & \boldsymbol{v}^T\end{bmatrix}^T$ and

$$\boldsymbol{A}(t) = \begin{bmatrix}\boldsymbol{0}_{3\times3} & \boldsymbol{I}_3 \\ \boldsymbol{G}(\bar{\boldsymbol{r}}) & \boldsymbol{0}_{3\times3}\end{bmatrix}, \quad \boldsymbol{B} = \begin{bmatrix}\boldsymbol{0}_{3\times3} \\ \boldsymbol{I}_3\end{bmatrix}, \tag{17}$$

with $\mathbf{0}_{n\times m}$ denoting the zero matrix in $\mathbb{R}^{n\times m}$. Using the second-order approximation in eq. (11), the solution over $[t_k, t_{k+1}]$ is

$$\delta\boldsymbol{x}_{k+1} = \boldsymbol{\Phi}(t_{k+1}, t_k)\,\delta\boldsymbol{x}_k + \int_{t_k}^{t_{k+1}} \boldsymbol{\Phi}(t_{k+1}, \tau)\boldsymbol{B}\,\delta\boldsymbol{a}_v(\tau)\,d\tau, \tag{18}$$

$$\approx \boldsymbol{\Phi}(t_{k+1}, t_k)\,\delta\boldsymbol{x}_k + \int_{t_k}^{t_{k+1}} \begin{bmatrix} \boldsymbol{I}_3(t_{k+1}-\tau) \\ \boldsymbol{I}_3 + \frac{1}{2}\boldsymbol{G}_k(t_{k+1}-\tau)^2 \end{bmatrix} \delta\boldsymbol{a}_v(\tau)\,d\tau, \tag{19}$$

where $\boldsymbol{G}_k = \boldsymbol{G}(\bar{\boldsymbol{r}}(t_k))$.

Given the nature of the vent disturbances, in this paper, $\boldsymbol{a}_v(t)$ is modeled as a Gaussian-Poisson point process. This modeling choice is motivated by the extensive literature on Poisson-process-based clutter modeling for target tracking [9, 10] and, more directly, by its application to the modeling of (un)-fortunate lack of acceleration knowledge (FLAK) events in [11]. For this type of model, impulses occur at random times $t_1, t_2, \ldots$, which follow a Poisson process with rate λ. This implies that the number of impulses in a given interval is Poisson-distributed, and the time between impulses is exponentially distributed with mean $1/\lambda$. In addition, each impulse has a random amplitude Δv, modeled as a Gaussian distribution with mean μ_v and variance σ_v^2. Furthermore, the direction of the impulse, expressed in the inertial frame and denoted by $\boldsymbol{u}_v^I(t)$, is assumed to be uncertain. While the characterization of the distribution of $\boldsymbol{u}_v^I(t)$ is developed in the following sections, it is assumed that $\boldsymbol{u}_v^I(t)$ possesses finite first and second moments,

$$\boldsymbol{d}(t) \triangleq \mathbb{E}\left[\boldsymbol{u}_v^I(t)\right], \quad \boldsymbol{D}(t) \triangleq \operatorname{cov}\left[\boldsymbol{u}_v^I(t)\right], \tag{20}$$

and is assumed independent of the event count, arrival times, and impulse magnitudes. Although the vent direction is a random variable, it is constrained to unit norm, $\|\boldsymbol{u}_v^I(t)\| = 1$. Therefore, the venting acceleration over a time interval Δt can be represented by the impulse train

$$\boldsymbol{a}_v(t) = \sum_{i=1}^{n_v} \Delta v_i\,\boldsymbol{u}_v^I(t)\,\delta(t-t_i) = \sum_{i=1}^{n_v} \left(\mu_v + \omega_v^{(i)}\right)\boldsymbol{u}_v^I(t)\,\delta(t-t_i), \tag{21}$$

where $n_v \sim \text{Poisson}(\lambda\Delta t)$ is the number of vents, $\omega_v^{(i)} \sim \mathcal{N}(0, \sigma_v^2)$ is the i-th perturbation from the nominal vent value, μ_v, and $\delta(t-t_i)$ is the Dirac delta distribution centered at time t_i.

4 Mean and Covariance Analysis of Venting Disturbances

Let the nominal trajectory be the estimated spacecraft state $\hat{\boldsymbol{x}}(t)$ propagated under vent-free dynamics,

$$\begin{aligned} \dot{\hat{\boldsymbol{r}}}(t) &= \hat{\boldsymbol{v}}(t), \\ \dot{\hat{\boldsymbol{v}}}(t) &= \boldsymbol{g}(\hat{\boldsymbol{r}}(t)). \end{aligned} \tag{22}$$

The estimation error and vent-acceleration perturbation are then

$$\delta\boldsymbol{x}(t) = \boldsymbol{x}(t) - \hat{\boldsymbol{x}}(t), \tag{23}$$

$$\delta\boldsymbol{a}_v(t) = \boldsymbol{a}_v(t). \tag{24}$$

Substituting eq. (21) into eq. (19) yields

$$\begin{aligned} \delta\boldsymbol{x}_{k+1} &\approx \boldsymbol{\Phi}(t_{k+1}, t_k)\, \delta\boldsymbol{x}_k \\ &\quad + \int_{t_k}^{t_{k+1}} \begin{bmatrix} \boldsymbol{I}_3(t_{k+1} - \tau) \\ \boldsymbol{I}_3 + \frac{1}{2}\boldsymbol{G}_k(t_{k+1} - \tau)^2 \end{bmatrix} \sum_{i=1}^{n_v} \left(\mu_v + \omega_v^{(i)}\right) \boldsymbol{u}_v^I(\tau)\, \delta(\tau - t_i)\, d\tau, \qquad (25) \\ &= \boldsymbol{\Phi}(t_{k+1}, t_k)\, \delta\boldsymbol{x}_k + \sum_{i=1}^{n_v} \left(\mu_v + \omega_v^{(i)}\right) \begin{bmatrix} \boldsymbol{I}_3(t_{k+1} - t_i) \\ \boldsymbol{I}_3 + \frac{1}{2}\boldsymbol{G}_k(t_{k+1} - t_i)^2 \end{bmatrix} \boldsymbol{u}_v^I(t_i), \qquad (26) \\ &= \boldsymbol{\Phi}(t_{k+1}, t_k)\delta\boldsymbol{x}_k + \boldsymbol{\eta}_k, \qquad (27) \end{aligned}$$

where the random variable

$$\boldsymbol{\eta}_k = \sum_{i=1}^{n_v} \left(\mu_v + \omega_v^{(i)}\right) \begin{bmatrix} \boldsymbol{I}_3(t_{k+1} - t_i) \\ \boldsymbol{I}_3 + \frac{1}{2}\boldsymbol{G}_k(t_{k+1} - t_i)^2 \end{bmatrix} \boldsymbol{u}_v^I(t_i) \tag{28}$$

represents the integrated effect of all venting events occurring over the propagation interval. Because the venting process generally possesses a non-zero mean, the expected estimation error does not necessarily vanish.

Define the mean error state as

$$\bar{\boldsymbol{m}}_k \triangleq \mathbb{E}[\delta\boldsymbol{x}_k]. \tag{29}$$

Taking the expectation of eq. (27) gives

$$\bar{\boldsymbol{m}}_{k+1} = \boldsymbol{\Phi}(t_{k+1}, t_k)\bar{\boldsymbol{m}}_k + \mathbb{E}\left[\boldsymbol{\eta}_k\right]. \tag{30}$$

This mean error is incorporated into the propagated state estimate according to

$$\hat{\boldsymbol{x}}_{k+1} = \hat{\boldsymbol{x}}_{k+1}^{\text{nom}} + \bar{\boldsymbol{m}}_{k+1}, \tag{31}$$

where $\hat{\boldsymbol{x}}_{k+1}^{\text{nom}}$ denotes the vent-free propagated state. Assuming that the state estimate is unbiased at time t_k, then $\bar{\boldsymbol{m}}_k = \mathbf{0}$, and eq. (31) reduces to

$$\hat{\boldsymbol{x}}_{k+1} = \hat{\boldsymbol{x}}_{k+1}^{\text{nom}} + \mathbb{E}\left[\boldsymbol{\eta}_k\right]. \tag{32}$$

In addition to the mean error, the uncertainty associated with the venting process must also be propagated. The covariance of the estimation error is defined as

$$\boldsymbol{P}_k = \mathbb{E}\left[\left(\delta\boldsymbol{x}_k - \bar{\boldsymbol{m}}_k\right)\left(\delta\boldsymbol{x}_k - \bar{\boldsymbol{m}}_k\right)^T\right]. \tag{33}$$

Assuming that $\boldsymbol{\eta}_k$ is independent of the error at time t_k, eq. (27) gives the covariance propagation

$$\boldsymbol{P}_{k+1} = \boldsymbol{\Phi}(t_{k+1}, t_k)\, \boldsymbol{P}_k\, \boldsymbol{\Phi}(t_{k+1}, t_k)^T + \boldsymbol{Q}_k, \tag{34}$$

where

$$\boldsymbol{Q}_k \triangleq \text{cov}[\boldsymbol{\eta}_k] \tag{35}$$

denotes the covariance of the integrated venting disturbance.

Therefore, propagation of the state estimate and its associated covariance requires the first two moments of the random variable $\boldsymbol{\eta}_k$. The following sections derive closed-form expressions for these moments.

4.1 Mean Venting Disturbance

Consider the integrated venting disturbance $\boldsymbol{\eta}_k$ defined in eq. (28). To evaluate its first moment, it is first noted that the vent direction $\boldsymbol{u}_v^I$ is assumed to remain constant over the propagation interval $[t_k, t_{k+1}]$. Consequently,

$$\boldsymbol{u}_v^I(t_i) = \boldsymbol{u}_{v,k}^I, \qquad \forall t_i \in [t_k, t_{k+1}], \tag{36}$$

and, from eq. (28), the integrated venting disturbance can be rewritten as

$$\boldsymbol{\eta}_k = \sum_{i=1}^{n_v} \left(\mu_v + \omega_v^{(i)}\right) \begin{bmatrix} \boldsymbol{I}_3(t_{k+1} - t_i) \\ \boldsymbol{I}_3 + \frac{1}{2}\boldsymbol{G}_k(t_{k+1} - t_i)^2 \end{bmatrix} \boldsymbol{u}_{v,k}^I. \tag{37}$$

The objective is now to compute the expected value of $\boldsymbol{\eta}_k$. Note that $\boldsymbol{\eta}_k$ is a compound random variable whose uncertainty arises from four components: the total number of venting events, their arrival times, the deviations of the vent magnitudes from their nominal value, and their directions. Applying the law of total expectation and exploiting the statistical independence of the vent magnitudes and directions from both the vent arrival times and the total number of venting events yields

$$\mathbb{E}[\boldsymbol{\eta}_k] = \mathbb{E}_{n_v}\left[\mathbb{E}_{t_i|n_v}\left[\mathbb{E}_{\omega_v}\left[\mathbb{E}_{\boldsymbol{u}_{v,k}^I}\left[\sum_{i=1}^{n_v}\left(\mu_v + \omega_v^{(i)}\right)\begin{bmatrix} \boldsymbol{I}_3(t_{k+1} - t_i) \\ \boldsymbol{I}_3 + \frac{1}{2}\boldsymbol{G}_k(t_{k+1} - t_i)^2 \end{bmatrix} \boldsymbol{u}_{v,k}^I\right]\right] \middle| n_v\right]\right], \tag{38}$$

$$= \mu_v \, \mathbb{E}_{n_v} \left[\mathbb{E}_{t_i|n_v} \left[\sum_{i=1}^{n_v} \begin{bmatrix} \boldsymbol{I}_3(t_{k+1} - t_i) \\ \boldsymbol{I}_3 + \frac{1}{2}\boldsymbol{G}_k(t_{k+1} - t_i)^2 \end{bmatrix} \middle| n_v \right] \right] \mathbb{E}_{\boldsymbol{u}^I_{v,k}} \left[\boldsymbol{u}^I_{v,k} \right], \tag{39}$$

where the fact that the perturbation is a zero mean Gaussian noise $\mathbb{E}[\omega_v^{(i)}] = 0$ is used. Conditioned on n_v, the vent arrival times are independent and identically distributed random variables uniformly distributed over the interval $[t_k, t_{k+1}]$ [12]. Therefore,

$$\mathbb{E}[\boldsymbol{\eta}_k] = \mu_v \, \mathbb{E}_{n_v}[n_v] \, \frac{1}{\Delta t_k} \int_{t_k}^{t_{k+1}} \begin{bmatrix} \boldsymbol{I}_3(t_{k+1} - \tau) \\ \boldsymbol{I}_3 + \frac{1}{2}\boldsymbol{G}_k(t_{k+1} - \tau)^2 \end{bmatrix} d\tau \, \mathbb{E}_{\boldsymbol{u}^I_{v,k}} \left[\boldsymbol{u}^I_{v,k} \right], \tag{40}$$

where $\Delta t_k = t_{k+1} - t_k$. Furthermore, recalling that $\mathbb{E}_{n_v}[n_v] = \lambda \Delta t_k$and from eq. (20) $\mathbb{E}_{\boldsymbol{u}^I_{v,k}}[\boldsymbol{u}^I_{v,k}] = \boldsymbol{d}_k$, the expectation simplifies to

$$\mathbb{E}[\boldsymbol{\eta}_k] = \lambda \mu_v \int_{t_k}^{t_{k+1}} \begin{bmatrix} \boldsymbol{I}_3(t_{k+1} - \tau) \\ \boldsymbol{I}_3 + \frac{1}{2}\boldsymbol{G}_k(t_{k+1} - \tau)^2 \end{bmatrix} d\tau \, \boldsymbol{d}_k, \tag{41}$$

Finally, evaluating the resulting integral yields the mean venting disturbance

$$\mathbb{E}[\boldsymbol{\eta}_k] = \lambda \mu_v \begin{bmatrix} \frac{\Delta t_k^2}{2} \boldsymbol{I}_3 \\ \Delta t_k \boldsymbol{I}_3 + \frac{\Delta t_k^3}{6} \boldsymbol{G}_k \end{bmatrix} \boldsymbol{d}_k. \tag{42}$$

4.2 Venting Disturbance Covariance

To evaluate the covariance of the integrated venting disturbance, it is convenient to express the contribution of each venting event separately. Define

$$\boldsymbol{X}_i \triangleq \left(\mu_v + \omega_v^{(i)} \right) \begin{bmatrix} \boldsymbol{I}_3(t_{k+1} - t_i) \\ \boldsymbol{I}_3 + \frac{1}{2}\boldsymbol{G}_k(t_{k+1} - t_i)^2 \end{bmatrix} \boldsymbol{u}^I_{v,k}, \tag{43}$$

such that the covariance of the integrated venting disturbance is

$$\operatorname{cov}(\boldsymbol{\eta}_k) = \mathbb{E}\left[\boldsymbol{\eta}_k \boldsymbol{\eta}_k^T\right] - \mathbb{E}[\boldsymbol{\eta}_k] \, \mathbb{E}[\boldsymbol{\eta}_k]^T, \tag{44}$$

$$= \mathbb{E}\left[\sum_{i=1}^{n_v} \boldsymbol{X}_i \sum_{i=1}^{n_v} \boldsymbol{X}_i^T \right] - \mathbb{E}[\boldsymbol{\eta}_k] \, \mathbb{E}[\boldsymbol{\eta}_k]^T. \tag{45}$$

The first expectation can be decomposed into the sum of the self-correlation and cross-correlation terms as

$$\mathbb{E}\left[\sum_{i=1}^{n_v}\boldsymbol{X}_i\sum_{i=1}^{n_v}\boldsymbol{X}_i^T\right]=\mathbb{E}\left[\sum_{i=1}^{n_v}\boldsymbol{X}_i\boldsymbol{X}_i^T\right]+\mathbb{E}\left[\sum_{\substack{i,j=1\\ i\neq j}}^{n_v}\boldsymbol{X}_i\boldsymbol{X}_j^T\right], \tag{46}$$

$$=\mathbb{E}_{n_v}\left[\mathbb{E}_{t_i|n_v}\left[\mathbb{E}_{\omega_v}\left[\mathbb{E}_{\boldsymbol{u}_{v,k}^I}\left[\sum_{i=1}^{n_v}\boldsymbol{X}_i\boldsymbol{X}_i^T\right]\right]\right]\middle| n_v\right] \tag{47}$$

$$+\mathbb{E}_{n_v}\left[\mathbb{E}_{t_i|n_v}\left[\mathbb{E}_{\omega_v}\left[\mathbb{E}_{\boldsymbol{u}_{v,k}^I}\left[\sum_{\substack{i,j=1\\ i\neq j}}^{n_v}\boldsymbol{X}_i\boldsymbol{X}_j^T\right]\right]\right]\middle| n_v\right]\right], \tag{48}$$

$$=\lambda(\mu_v^2+\sigma_v^2)\int_{t_k}^{t_{k+1}}\boldsymbol{\psi}(t_{k+1},\tau)\mathbb{E}\left[\boldsymbol{u}_{v,k}^I\left(\boldsymbol{u}_{v,k}^I\right)^T\right]\boldsymbol{\psi}(t_{k+1},\tau)^T\,d\tau \tag{49}$$

$$+\lambda^2\mu_v^2\int_{t_k}^{t_{k+1}}\boldsymbol{\psi}(t_{k+1},\tau)d\tau\,\mathbb{E}\left[\boldsymbol{u}_{v,k}^I\left(\boldsymbol{u}_{v,k}^I\right)^T\right]\int_{t_k}^{t_{k+1}}\boldsymbol{\psi}(t_{k+1},\tau)^T\,d\tau. \tag{50}$$

Introducing the covariance of the vent direction,

$$\operatorname{cov}\left[\boldsymbol{u}_{v,k}^I\right]=\boldsymbol{D}_k=\mathbb{E}\left[\boldsymbol{u}_{v,k}^I\left(\boldsymbol{u}_{v,k}^I\right)^T\right]-\boldsymbol{d}_k\boldsymbol{d}_k^T, \tag{51}$$

allows the process noise covariance to be written as

$$\boldsymbol{Q}_k=\lambda^2(\mu_v^2+\sigma_v^2)\int_{t_k}^{t_{k+1}}\boldsymbol{\psi}(t_{k+1},\tau)\left(\boldsymbol{D}_k+\boldsymbol{d}_k\boldsymbol{d}_k^T\right)\boldsymbol{\psi}(t_{k+1},\tau)^T\,d\tau \tag{52}$$

$$+\lambda^2\mu_v^2\int_{t_k}^{t_{k+1}}\boldsymbol{\psi}(t_{k+1},\tau)d\tau\,\boldsymbol{D}_k\int_{t_k}^{t_{k+1}}\boldsymbol{\psi}(t_{k+1},\tau)^T\,d\tau. \tag{53}$$

Evaluating the preceding integrals yields the following block components of the venting disturbance covariance matrix:

$$\boldsymbol{Q}_k^{(1:3,1:3)}=\lambda(\mu_v^2+\sigma_v^2)\frac{\Delta t_k^3}{3}\left(\boldsymbol{D}_k+\boldsymbol{d}_k\boldsymbol{d}_k^T\right)+\lambda^2\mu_v^2\frac{\Delta t_k^4}{4}\boldsymbol{D}_k, \tag{54}$$

$$\boldsymbol{Q}_k^{(1:3,4:6)}=\lambda(\mu_v^2+\sigma_v^2)\left(\frac{\Delta t_k^2}{2}\left(\boldsymbol{D}_k+\boldsymbol{d}_k\boldsymbol{d}_k^T\right)+\frac{\Delta t_k^4}{8}\left(\boldsymbol{D}_k+\boldsymbol{d}_k\boldsymbol{d}_k^T\right)\boldsymbol{G}_k^T\right)$$

$$+\lambda^2\mu_v^2\left(\frac{\Delta t_k^3}{2}\boldsymbol{D}_k+\frac{\Delta t_k^5}{12}\boldsymbol{D}_k\boldsymbol{G}_k^T\right), \tag{55}$$

$$\begin{aligned}\boldsymbol{Q}_k^{(4:6,4:6)} =& \lambda(\mu_v^2+\sigma_v^2)\Delta t_k\left(\boldsymbol{D}_k+\boldsymbol{d}_k\boldsymbol{d}_k^T\right)\\ &+\lambda(\mu_v^2+\sigma_v^2)\left(\frac{\Delta t_k^3}{6}\left(\left(\boldsymbol{D}_k+\boldsymbol{d}_k\boldsymbol{d}_k^T\right)\boldsymbol{G}_k^T+\boldsymbol{G}_k\left(\boldsymbol{D}_k+\boldsymbol{d}_k\boldsymbol{d}_k^T\right)\right)\right)\\ &+\lambda(\mu_v^2+\sigma_v^2)\frac{\Delta t_k^5}{20}\boldsymbol{G}_k\left(\boldsymbol{D}_k+\boldsymbol{d}_k\boldsymbol{d}_k^T\right)\boldsymbol{G}_k^T\\ &+\lambda^2\mu_v^2\left(\Delta t_k^2\boldsymbol{D}_k+\frac{\Delta t_k^4}{6}\left(\boldsymbol{G}_k\boldsymbol{D}_k+\boldsymbol{D}_k\boldsymbol{G}_k^T\right)+\frac{\Delta t_k^6}{36}\boldsymbol{G}_k\boldsymbol{D}_k\boldsymbol{G}_k^T\right),\end{aligned} \tag{56}$$

with $\boldsymbol{Q}_k^{(4:6,1:3)}=\boldsymbol{Q}_k^{(1:3,4:6)T}$. Here, the subscript $(a{:}b,c{:}d)$ denotes the block formed by rows a through b and columns c through d.

5 Numerical Examples

This section presents six MC examples, involving a spacecraft in a near-rectilinear halo orbit (NRHO) around the Moon, to test the proposed framework. In these examples, the spacecraft motion is modeled using the circular restricted three body problem (CR3BP) [8], with the continuous-time dynamics given by

$$\begin{aligned}\dot{x} &= v_x,\\ \dot{y} &= v_y,\\ \dot{z} &= v_z,\\ \dot{v}_x &= 2v_y+x-\frac{1-\mu}{r_1^3}(x+\mu)-\frac{\mu}{r_2^3}(x-1+\mu),\\ \dot{v}_y &= -2v_x+y-\frac{1-\mu}{r_1^3}y-\frac{\mu}{r_2^3}y,\\ \dot{v}_z &= -\frac{1-\mu}{r_1^3}z-\frac{\mu}{r_2^3}z,\end{aligned} \tag{57}$$

where (x,y,z) and (v_x,v_y,v_z) denote the spacecraft position and velocity components, respectively, in the Earth–Moon barycentric rotating frame, μ is the Earth–Moon mass parameter, and

$$r_1=\sqrt{(x+\mu)^2+y^2+z^2},\qquad r_2=\sqrt{(x-1+\mu)^2+y^2+z^2}, \tag{58}$$

are the distances from the spacecraft to the Earth and the Moon, respectively. Thus, instead of using an inertial frame, the venting disturbances are modeled with respect to the barycenter synodic frame. The nonlinear dynamics are propagated numerically using a Runge–Kutta integration scheme [13].

To assess the proposed methodology, 1000 MC simulations are performed for each example. Each MC run is propagated for 6 days, nearly completing a full orbit, and

the estimated state and covariance are propagated with a time step of 60 seconds. The initial true state is sampled according to

$$\boldsymbol{x}_0 \sim \mathcal{N}(\bar{\boldsymbol{x}}_0, \boldsymbol{P}_0)\,, \tag{59}$$

where $\bar{\boldsymbol{x}}_0$ corresponds to the approximate apolune of the southern 9:2 NRHO,

$$\bar{\boldsymbol{x}}_0 = \left[394925.02 \text{ km},\ 0 \text{ km},\ -68353.90 \text{ m},\ 0 \text{ m/s},\ -85.16 \text{ m/s},\ 0 \text{ m/s}\right]^T \tag{60}$$

and $\boldsymbol{P}_0$ is given by

$$\boldsymbol{P}_0 = \begin{bmatrix} (100 \text{ m})^2 \boldsymbol{I}_3 & \boldsymbol{0}_{3\times 3} \\ \boldsymbol{0}_{3\times 3} & (0.01 \text{ m/s})^2 \boldsymbol{I}_3 \end{bmatrix}. \tag{61}$$

The numerical results are organized into two sets of three examples. The first set investigates the validity and robustness of the instantaneous-impulse assumption used to model venting disturbances, while the second set examines the effect of attitude uncertainty.

The first two examples focus primarily on PSA vents, which refer to the air revitalization that control humidity and CO_2 onboard. These types of vents have a different magnitude depending on whether the astronauts are exercising, awake, or sleeping. The first example is used to validate the analytic covariance propagation derived in section 4. Therefore, in this example, the vents are modeled as an instantaneous impulse in both the truth model and the analytic propagation, with the goal of showing that the true and predicted uncertainty match. The second example tests the analytic model in a more realistic case, where the PSA vents in the truth model are not instantaneous impulses but finite-duration perturbations. The third example focuses on WW vents, which usually happen when the onboard tank reaches capacity. This type of vent has a longer duration than the PSA vents, although it occurs less frequently, making it a good example to test the robustness of the instantaneous impulse assumption.

It is important to note that true vents produce an initial transient thrust that decays to a steady-state value. The characteristics of this initial transient are determined by the physics of the venting mechanism itself. In contrast, the steady-state thrust depends on crew metabolic activity. For example, during exercise, higher metabolic rates lead to increased CO_2 production, resulting in a stronger steady-state venting value. For simulation purposes, however, this paper considers only two simplified vent profiles, namely instantaneous impulses and finite-duration perturbations. In both cases, the total Δv induced by a vent is kept the same, whether it occurs as an instantaneous impulse or over a finite duration.

In the first three examples, the vent direction is assumed to be perfectly known, thereby isolating the effects associated with the temporal representation of the vent disturbance. The fourth through sixth examples instead focus on the effect of attitude uncertainty. In these cases, only PSA vents modeled as instantaneous impulses are considered, allowing the analysis to isolate the impact of uncertainty in the vent direction. Three different attitude uncertainty models are investigated. The first assumes that the attitude error is Gaussian distributed. The second models the vent direction

as uniformly distributed over the sphere of unit radius. The third represents the attitude error using a first-order Gauss–Markov process. Together, these examples assess the ability of the proposed covariance propagation framework to capture the effects of different statistical representations of attitude uncertainty on the spacecraft state uncertainty.

The remainder of this section is organized as follows. First, the MC analysis methodology used to assess the proposed analytic covariance propagation is described. The subsequent subsections then present each of the six numerical examples in turn.

5.1 Monte Carlo Preliminaries

Since MC analysis is the primary tool for the validation of the proposed work, this section provides the preliminaries needed to perform the numerical analysis. In a MC simulation, a large number of trajectories (or scenarios) are tested. In each scenario, there is a truth trajectory, denoted by $\boldsymbol{x}$, and an estimated trajectory, denoted by $\hat{\boldsymbol{x}}$. The truth trajectory starts from an initial value (usually the mean of a Gaussian distribution) and is propagated with what is called the truth model. The estimated trajectory starts from a random value, sampled from the Gaussian distribution of the initial value of the truth trajectory. The estimated trajectory is propagated with an estimated model of the truth, and an estimate of its uncertainty is calculated.

From the MC trajectories, various statistics can be analyzed to evaluate the estimation technique used to obtain the estimated trajectory. The mean squared error (MSE) is a common way of evaluating estimation techniques and is defined as

$$\mathrm{MSE}(t_k) = \mathbb{E}\left[\delta\boldsymbol{x}(t_k)^T \delta\boldsymbol{x}(t_k)\right], \tag{62}$$

where, as defined in eq. (23), $\delta\boldsymbol{x}(t_k)$ is the estimation error at time step k, and the expectation can be evaluated via the sample mean of the MC trajectories. The sample covariance of the estimation error is defined as

$$\begin{aligned}\boldsymbol{P}_{\mathrm{samp}}(t_k) &= \mathbb{E}\left[\left(\delta\boldsymbol{x}(t_k) - \overline{\delta\boldsymbol{x}}(t_k)\right)\left(\delta\boldsymbol{x}(t_k) - \overline{\delta\boldsymbol{x}}(t_k)\right)^T\right] &(63)\\ &= \mathbb{E}\left[\delta\boldsymbol{x}(t_k)\delta\boldsymbol{x}(t_k)^T\right] - \overline{\delta\boldsymbol{x}}(t_k)\overline{\delta\boldsymbol{x}}(t_k)^T, &(64)\end{aligned}$$

where the first term represents the mean square of the estimation error, and the second term is the squared estimation bias. In this notation, $\overline{\delta\boldsymbol{x}}(t_k)$ is the sample mean of the estimation error (obtained via the MC trajectories). When the estimate is unbiased, i.e., $\overline{\delta\boldsymbol{x}}(t_k) = 0$, the sample covariance reduces to a mean square-type definition.

In this paper, the estimated uncertainty is represented by the estimation error covariance, as derived in section 4. This derivation assumes that the estimation error is unbiased, which is a common assumption in Kalman filtering. Accordingly, the estimation error covariance is defined as

$$\boldsymbol{P}(t_k) = \mathbb{E}\left[\delta\boldsymbol{x}(t_k)\delta\boldsymbol{x}(t_k)^T\right], \tag{65}$$

where the right-hand side is not available in practice, since the true trajectories are unknown to the estimation technique, and thus $\boldsymbol{P}(t_k)$ is calculated directly. Therefore,

for the propagation scheme designed in this work to be consistent, the MC sample mean of the estimation error covariance should approximately match the mean square of the estimation error.

For a practical implementation, the following quantities are compared. First, note that for each MC trajectory, there is an associated estimation error covariance at each time step. Thus, the sample mean of the estimation error covariance is compared against the mean square of the estimation error, such that

$$\frac{1}{n_{\mathrm{MC}}} \sum_{i=1}^{n_{\mathrm{MC}}} \boldsymbol{P}^{(i)}(t_k) \approx \frac{1}{n_{\mathrm{MC}}} \sum_{i=1}^{n_{\mathrm{MC}}} \delta\boldsymbol{x}^{(i)}(t_k) \delta\boldsymbol{x}^{(i)}(t_k)^T, \tag{66}$$

where $\boldsymbol{P}^{(i)}(t_k)$ is the estimation error covariance at time step k for MC run i, and $\delta\boldsymbol{x}^{(i)}(t_k)$ is the estimation error at time step k for MC run i. If these two quantities match (in a matrix sense), the estimate is unbiased, and the estimation error covariance is consistent with the mean square of the estimation error. Note that, for the results to have statistical significance, a large number of MC trajectories should be performed.

5.2 Pressure Swing Adsorption Vents as Instantaneous Impulses

As mentioned earlier, this first example is used to validate the covariance propagation derived in section 4. In this example and the two that follow, the vent direction is assumed to be perfectly known. In particular, the vent direction expressed in the inertial frame can be written as

$$\boldsymbol{u}_v^I(t) = \boldsymbol{T}_B^I(t)\, \boldsymbol{u}_v^B, \tag{67}$$

where $\boldsymbol{u}_v^B$is the vent direction expressed in the body frame and $\boldsymbol{T}_B^I(t)$ is the direction cosine matrix (DCM) transforming vectors from the body frame to the inertial frame at time t. For these three examples, $\boldsymbol{T}_B^I(t)$ is obtained from the transformation between the radial-transverse-normal (RTN) and rotating frames, with the transformation matrix calculated from the true state. The same transformation is used for both the truth model and the propagation of the state estimate and covariance.

For the venting disturbances, three types of vents are considered in this case, corresponding to astronauts exercising, performing daily activities, and sleeping. Vent directions and mean time of arrival are taken from Joshi et al. [4, 5]. In practice, the same venting hardware would be used regardless of the crew's current activity. However, in order to test different orientations, different venting directions are leveraged for the crew's awake, asleep, and exercise periods. Table 1 shows the venting parameters for each vent type considered.

As mentioned before, for this example, the true state is perturbed with random vents modeled as instantaneous impulses. Figure 1 shows the types of vents used in the simulation. Again, this work departs from reality and assumes that all three vents (corresponding to the crew's awake, asleep, and exercise periods) are active simultaneously to thoroughly stress the filter. It is important to note that this figure

Table 1 PSA Vent Parameters

Vent Type	μ_v [m/s]	σ_v [m/s]	λ [1/s]	$\boldsymbol{u}_v^B$ [n.d.]
Exercise	0.0015	$\mu_v/9$	1/200	$[0.500\ 0.866\ \ 0.000]^T$
Awake	0.0025	$\mu_v/9$	1/900	$[0.500\ 0.091\ -0.861]^T$
Sleep	0.0034	$\mu_v/9$	1/1800	$[0.500\ 0.826\ \ 0.260]^T$

only shows the vents for one day in the simulation, but the vents remain *on* for the entire simulation.

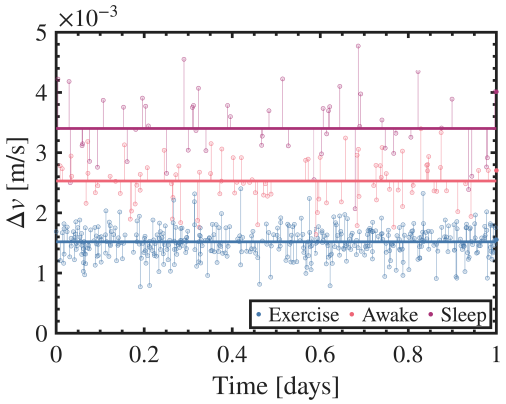


Fig. 1 True vent profile (PSA), modeled as instantaneous impulses, for one day of the simulation. The solid lines represent the nominal vent values.

Figure 2 shows the standard deviation profiles [14] and the sample standard deviation as a function of time. That is, the trace of the left-hand side of eq. (66), denoted as `Filter` σ, and the trace of the right-hand side of eq. (66), denoted as `Sample` σ. From this figure, it can be seen that the standard deviation profiles match the sample standard deviation. This suggests that the covariance propagation, as derived in section 4, is correct and yields consistent results. It is also important to note that the covariance propagation remains consistent near the perilune, approximately at 3 days, where the most nonlinear effects in the dynamics occur. This result validates the covariance propagation when the vents in the truth model are modeled as instantaneous impulses.

Figure 3 shows the estimation error plots for each component of the state. For each subplot, the estimation error and its corresponding sample mean are shown in gray and black, respectively. In addition, the estimated error variance is compared with the mean square of the estimation error for each component. From this figure, two key conclusions can be made. First, it can be seen that the estimation error is close to zero, suggesting an unbiased estimator. And second, the predicted (or estimated) variance matches the corresponding mean square of the estimation error. From this, it can be seen that the propagation is consistent when the true vent profile matches the assumption of treating vents as instantaneous impulses.

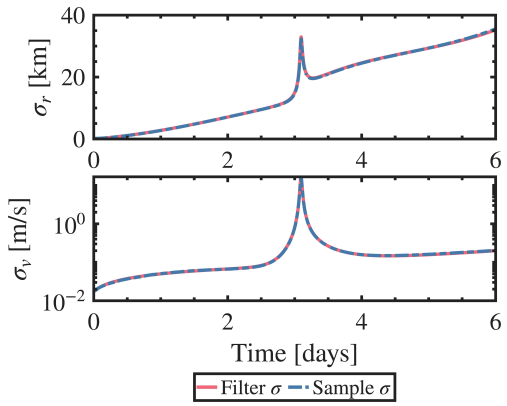


Fig. 2 Standard deviation profiles as a function of time for the true vents (PSA) modeled as instantaneous impulses. The red solid line shows the sample standard deviation. The blue dashed line shows the predicted standard deviation.

5.3 Pressure Swing Adsorption Vents as Finite Perturbations

From the example in section 5.2, it was shown that when the vents are instantaneous impulses, the covariance propagation derived in section 4 is consistent. However, as mentioned before, vents are not impulses. In crewed spacecraft, vents can produce finite perturbations, meaning they act over a period of time rather than instantaneously. This example shows that by approximating finite-duration vents as instantaneous impulses, and using the framework in section 4, the covariance growth can still be tracked accurately.

Therefore, for the truth model, the vents are now modeled as

$$a_v(t) = \sum_{i=1}^{n_v} \left(\mu_a + \omega_a^{(i)}\right) \mathcal{U}(t_i, \Delta t_a), \tag{68}$$

where $\mu_a = \mu_v/\Delta t_a$ is the nominal vent value, $\omega_a^{(i)} \sim \mathcal{N}(0, \sigma_u^2)$ with $\sigma_u^2 = \sigma_a^2/\Delta t_a^2$, and Δt_a is the vent duration, such that

$$\mathcal{U}(t_i, \Delta t_a) = \begin{cases} 1 & t_i \leq t \leq t_i + \Delta t_a, \\ 0 & \text{otherwise.} \end{cases} \tag{69}$$

Note that in Joshi et al. [5], different profiles for the vents are studied. However, for this work, only rectangular profiles are considered. In the context of the estimated state and covariance propagation, as per section 4, the vents are still treated as impulses, resulting in a mismatch between the truth model and the estimated model.

Similar to section 5.2, for this example, the same three PSA vents are considered simulating astronauts exercising, performing daily activities, and sleeping. Vent directions and mean arrival time remain the same. The vent duration is set to 2 seconds for all vents, that is $\Delta t_a = 2$ s. Figure 4 shows the true vent profile used for this example, for one day of the simulation. While the figure only shows the vents for one day in

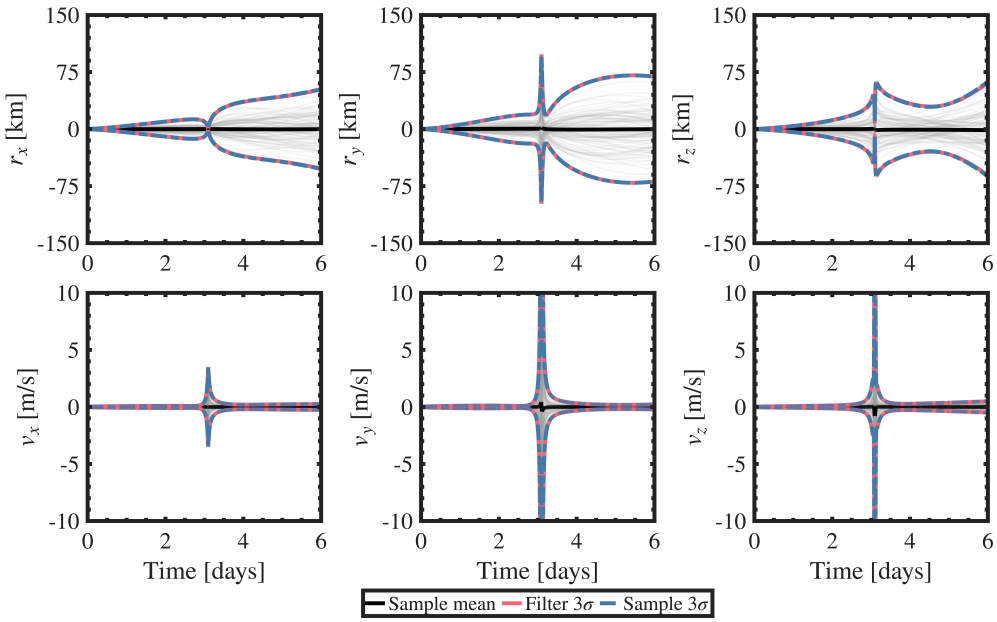


Fig. 3 Estimation error as a function of time for the true vents (PSA) modeled as instantaneous impulses. The gray lines show the estimation error for each MC. The solid black shows the sample error mean. The red solid line shows the estimated error variance, and the dashed blue line shows the mean square of the estimation error.

the simulation, the vents also remain *on* for the entire simulation. Note that in this case, the vents are not overlapping, simulating a more realistic scenario in which the astronauts are not exercising, awake, and sleeping at the same time.

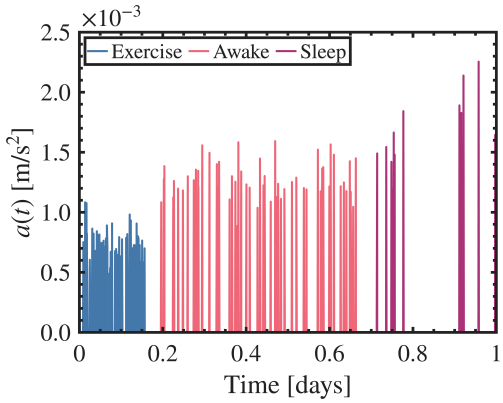


Fig. 4 True vent profile (PSA), modeled as finite perturbations, for one day of the simulation.

In this case, a state and covariance update is assumed to happen once per day. This assumption reflects the goal of this section, which is to test more realistic scenarios that could occur during a mission. As a result, after each day, the estimated state and covariance are reset to match the initial covariance used to generate the true state. Also in this example, the vent direction in the inertial frame is assumed to be perfectly known.

Figure 5 shows the standard deviation profiles and the sample standard deviation as a function of time (the trace of the left-hand side of eq. (66), denoted as `Filter` σ, and the trace of the left-hand side of eq. (66), denoted as `Sample` σ). Just like in section 5.2, this figure shows that the covariance propagation represents the error growth accurately. Nevertheless, because the finite perturbations are approximated as impulses, the propagated covariance is slightly optimistic. In this example, the drops seen after each day are due to the assumed state and covariance update.

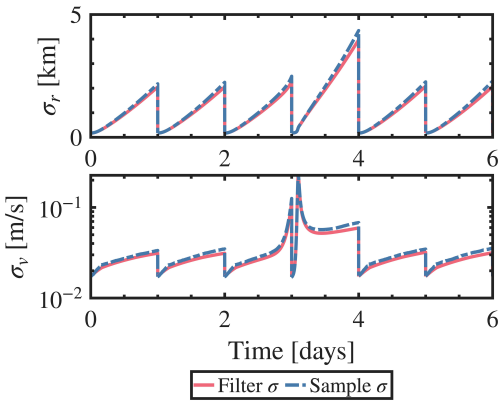


Fig. 5 Standard deviation profiles as a function of time for the true vents (PSA) modeled as finite perturbations. The red solid line shows the sample standard deviation. The blue dashed line shows the predicted standard deviation.

Figure 6 provides an explanation for the slight overconfidence seen in fig. 5. Note that in this case, the estimation error is biased. Since the analytical covariance assumes that the state estimate is unbiased, eq. (34) is unable to capture both the uncertainty and the bias. Nonetheless, the mismatch between the estimated and the sample errors is small and can easily be fixed if state updates occur more frequently (as the estimate would drift less from the truth, fitting the unbiasedness requirement).

5.4 Waste Water Vents as Finite Perturbations

In the previous sections, the analytical covariance propagation was tested using two different examples. The first demonstrated that the proposed framework performs well when the truth model treats vents as instantaneous impulses. The second showed that modeling finite vents as instantaneous impulses can still yield accurate covariance propagation. In this section, the consistency of the propagation is tested for longer vent durations.

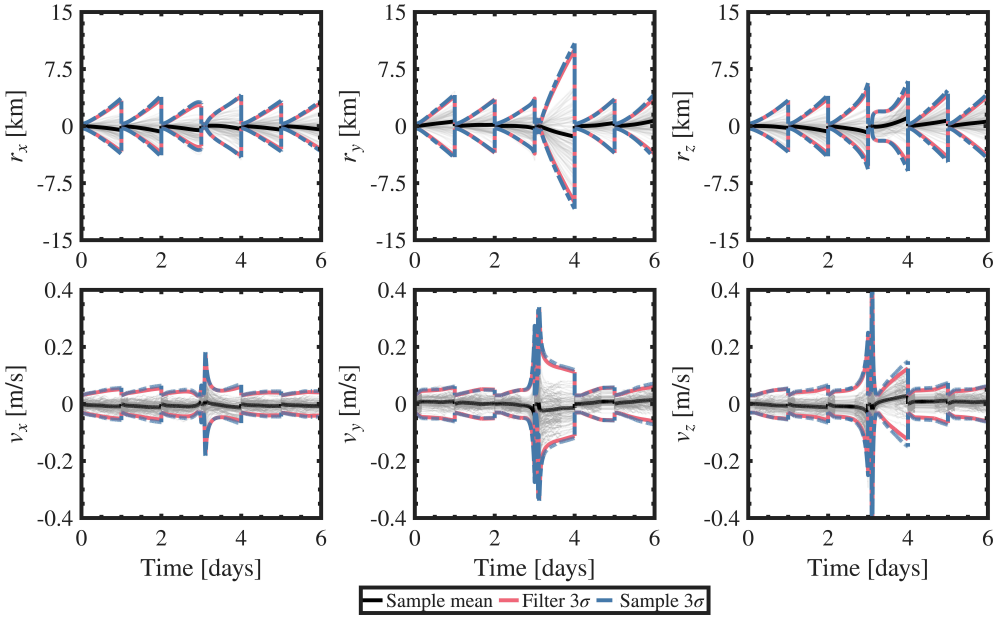


Fig. 6 Estimation error as a function of time for the true vents (PSA) modeled as finite perturbations. The gray lines show the estimation error for each MC. The solid black shows the sample error mean. The red solid line shows the estimated error variance, and the dashed blue line shows the mean square of the estimation error.

For this example, the focus now shifts to WW vents. These vents are particularly interesting, as they can last up to 8.6 minutes but occur less frequently than PSA vents. Table 2 lists the vent parameters used in this section, taken from Joshi et al [4, 5]. Figure 7 shows the true vent profile in this example, for one day of the simulation. As with the other examples, while the figure only shows the vents for one day in the simulation, the vents also remain *on* for the entire simulation. Note that in this case, even though the vents last for a significantly longer duration, the mean time of arrival is much more spread out. As a reminder, for this example, there is a mismatch between the truth model and the estimated model. For the estimated state and covariance propagation, the vents are still treated as instantaneous impulses, whereas for the truth, the vents are finite perturbations lasting for $\Delta t_a = 8.6$ mins.

Table 2 WW Vent Parameters

Vent Type	μ_v (m/s)	σ_v (m/s)	λ (1/hr)	$\boldsymbol{u}_v^B$ (n.d.)
Waste Water	0.0040	$\mu_v/9$	1/6	$[0.500\ 0.091\ -0.861]^T$

For this case, each MC scenario is configured as in section 5.3, with the only difference being the replacement of PSA vents by WW vents. Figure 8 shows the

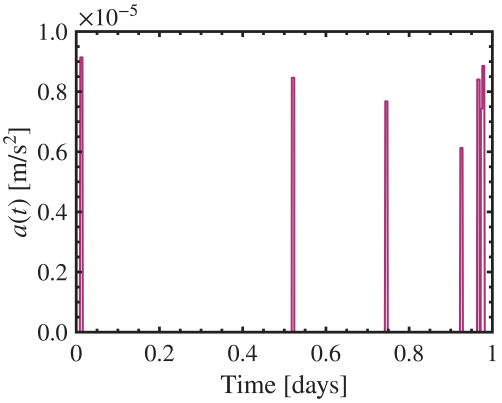


Fig. 7 True vent profile (WW), modeled as finite perturbations, for one day of the simulation.

standard deviation profiles as a function of time, and the estimation error plots can be seen in fig. 9. From these figures, it can be seen that, even though the WW vents last longer than the PSA vents, the analytic propagation still works as the standard deviation profiles match and the estimation error remains zero mean for the entire simulation. This is due to the fact that the WW vents are more infrequent, and its amplitude is smaller as they are spread out over a longer duration, which allows the impulse assumption to be a good approximation for the entire simulation.

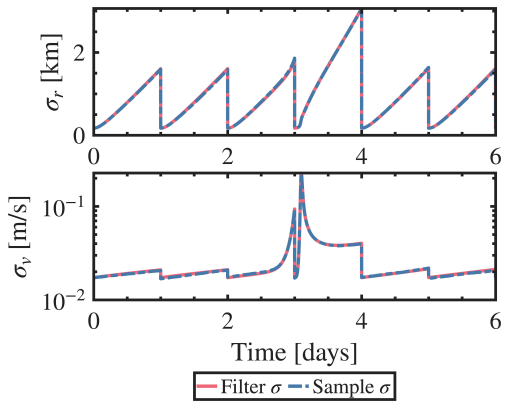


Fig. 8 Standard deviation profiles as a function of time for the true vents (WW) modeled as finite perturbations. The red solid line shows the sample standard deviation. The blue dashed line shows the predicted standard deviation.

5.5 Attitude Error as a Gaussian Noise

As discussed previously, the first three examples analyzed the instantaneous-impulse assumption introduced in section 4 under the assumption of perfect knowledge of the vent direction. In this section and the two that follow, the focus shifts to the

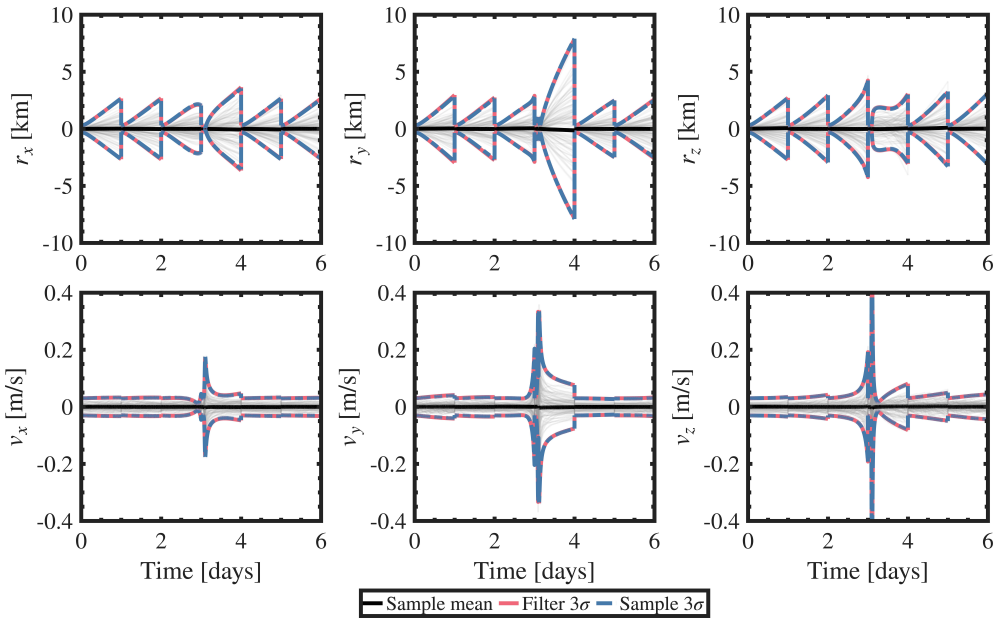


Fig. 9 Estimation error as a function of time for the true vents (WW) modeled as finite perturbations. The gray lines show the estimation error for each MC. The solid black shows the sample error mean. The red solid line shows the estimated error variance, and the dashed blue line shows the mean square of the estimation error.

characterization and analysis of uncertainty in the vent direction. Only PSA vents modeled as instantaneous impulses are considered, both in the truth model and in the estimated model. Thus, the setup is identical to that of section 5.2, with the exception that the vent direction is now uncertain.

In this first example, the uncertainty in the vent direction is attributed to uncertainty in the spacecraft attitude. The vent direction expressed in the inertial frame at time t_k is therefore given by

$$\boldsymbol{u}_{v,k}^{I} = \exp\left(-[\delta\boldsymbol{\alpha}_k]^{\times}\right) \bar{\boldsymbol{T}}_{B,k}^{I} \boldsymbol{u}_{v}^{B}, \tag{70}$$

where $[\boldsymbol{a}]^{\times}$ denotes the skew-symmetric matrix associated with the cross product with $\boldsymbol{a}$, $\bar{\boldsymbol{T}}_{B,k}^{I}$ is the known nominal direction cosine matrix transforming vectors from the spacecraft body frame to the inertial frame at time t_k, $\boldsymbol{u}_{v}^{B}$ is the vent direction expressed in the spacecraft body frame, and $\delta\boldsymbol{\alpha}_k$ represents the attitude error. The attitude error is modeled as a zero-mean Gaussian random vector,

$$\delta\boldsymbol{\alpha}_k \sim \mathcal{N}\left(\boldsymbol{0}, \sigma_a^2 \boldsymbol{I}_3\right), \qquad \mathbb{E}\left[\delta\boldsymbol{\alpha}_k \delta\boldsymbol{\alpha}_{k+1}^{T}\right] = \boldsymbol{0}_{3\times 3}, \tag{71}$$

where σ_a^2 denotes the variance of each component of the attitude error. The second condition indicates that the attitude errors at different time steps are uncorrelated.

As in the previous examples, the nominal direction cosine matrix $\bar{\boldsymbol{T}}^I_{B,k}$ is obtained from the transformation between the RTN and rotating frames and is calculated from the true state at time t_k. The same nominal transformation is used for both the truth model and the propagation of the state estimate and covariance. Throughout this example, the attitude uncertainty is characterized by a standard deviation of $\sigma_a = 10$ deg. Application of the mean and covariance framework developed in section 4 requires the first two moments of the random vent direction $\boldsymbol{u}^I_{v,k}$. To derive these quantities, recall the Taylor series expansion of the exponential map,

$$\exp\bigl(-[\delta\boldsymbol{\alpha}_k]_\times\bigr) \approx \boldsymbol{I}_3 - [\delta\boldsymbol{\alpha}_k]_\times + \frac{1}{2}[\delta\boldsymbol{\alpha}_k]^2_\times - \frac{1}{3}[\delta\boldsymbol{\alpha}_k]^3_\times + \cdots . \tag{72}$$

A first-order approximation of the exponential map is initially adopted, yielding

$$\boldsymbol{u}^I_{v,k} = \bigl(\boldsymbol{I}_3 - [\delta\boldsymbol{\alpha}_k]_\times\bigr)\,\bar{\boldsymbol{T}}^I_{B,k}\,\boldsymbol{u}^B_v = \bar{\boldsymbol{T}}^I_{B,k}\,\boldsymbol{u}^B_v + \Bigl[\bar{\boldsymbol{T}}^I_{B,k}\,\boldsymbol{u}^B_v\Bigr]_\times \delta\boldsymbol{\alpha}_k. \tag{73}$$

The corresponding first and second moments of the vent direction are then obtained as

$$\boldsymbol{d}_k = \mathbb{E}\bigl[\boldsymbol{u}^I_{v,k}\bigr] = \bar{\boldsymbol{T}}^I_{B,k}\,\boldsymbol{u}^B_v, \tag{74}$$

$$\begin{aligned}
\boldsymbol{D}_k &= \operatorname{cov}\bigl[\boldsymbol{u}^I_{v,k}\bigr], && (75)\\
&= \mathbb{E}\left[\Bigl[\bar{\boldsymbol{T}}^I_{B,k}\,\boldsymbol{u}^B_v\Bigr]_\times \delta\boldsymbol{\alpha}_k\delta\boldsymbol{\alpha}_k^T \Bigl[\bar{\boldsymbol{T}}^I_{B,k}\,\boldsymbol{u}^B_v\Bigr]^T_\times\right], && (76)\\
&= \sigma_a^2\Bigl[\bar{\boldsymbol{T}}^I_{B,k}\,\boldsymbol{u}^B_v\Bigr]_\times \Bigl[\bar{\boldsymbol{T}}^I_{B,k}\,\boldsymbol{u}^B_v\Bigr]^T_\times . && (77)
\end{aligned}$$

The results obtained using the first-order approximation are shown in figs. 10 and 11. It is evident that the estimated mean exhibits a noticeable bias, causing the filter to become overly optimistic. This indicates that the filter is no longer statistically consistent. This discrepancy arises because the first-order approximation neglects the second-order contribution to the mean of the vent direction expressed in the inertial frame.

To account for this effect, the mean vent direction is instead approximated using the second-order expansion of the exponential map, leading to

$$\boldsymbol{u}^I_{v,k} = \left(\boldsymbol{I}_3 - [\delta\boldsymbol{\alpha}_k]_\times + \frac{1}{2}[\delta\boldsymbol{\alpha}_k]^2_\times\right)\bar{\boldsymbol{T}}^I_{B,k}\,\boldsymbol{u}^B_v. \tag{78}$$

Using the identity $[\boldsymbol{a}]^2_\times = \boldsymbol{a}\boldsymbol{a}^T - \|\boldsymbol{a}\|^2\boldsymbol{I}_3$,

$$\mathbb{E}\Bigl[[\delta\boldsymbol{\alpha}_k]^2_\times\Bigr] = -2\sigma_a^2\boldsymbol{I}_3, \tag{79}$$

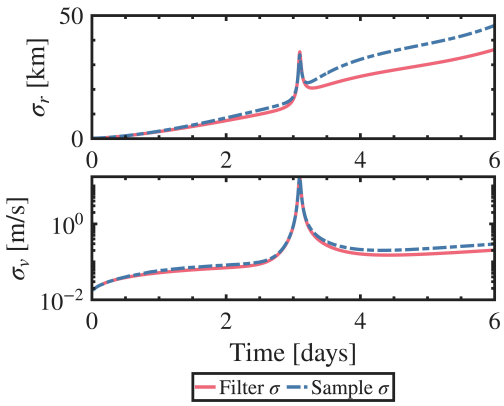


Fig. 10 Standard deviation profiles as a function of time for the attitude error modeled as Gaussian noise and using a first-order approximation in the filter. The red solid line shows the sample standard deviation. The blue dashed line shows the predicted standard deviation.

and therefore the mean of the venting direction using a second-order Taylor expansion is

$$\boldsymbol{d}_k = \left(1 - \sigma_a^2\right) \bar{\boldsymbol{T}}_{B,k}^{I} \, \boldsymbol{u}_v^B. \tag{80}$$

The corresponding results are presented in figs. 12 and 13. In contrast to the first-order approximation, the second-order approximation accurately predicts the mean of the vent disturbance, resulting in excellent agreement with the MC simulations. Furthermore, the covariance predicted by the filter matches the sample covariance accurately, showing that no second-order approximation is needed to compute the covariance of the venting direction. This behavior can be explained by the results in [15], which show that a second-order Taylor series expansion introduces terms of order σ_a^4 in the covariance expression. Assuming $\sigma_a < 1$, these higher-order terms are negligible compared to the terms of order σ_a^2, and therefore have a negligible impact on the resulting covariance. These results demonstrate that, in this example, retaining the second-order terms in the mean propagation is essential for maintaining filter consistency. In contrast, these terms can be omitted from the covariance propagation without compromising performance.

5.6 Uniformly Distributed Vent Direction

In this example, the vent direction is assumed to be uniformly distributed over the unit sphere. Thus, at each time instant, the vent direction may point in any direction with equal probability, and the vent directions at different time instants are assumed to be uncorrelated. This represents a limiting case in which no information about the spacecraft attitude is available. Although such an assumption may be overly conservative for practical applications, it provides a useful edge case for evaluating the proposed framework under maximal directional uncertainty.

To mathematically characterize the distribution of the unit vector, consider the rotational invariance of a uniform distribution. Specifically, if a unit vector is uniformly distributed over the sphere, then its distribution remains unchanged under any rotation. This property can be formally characterized using the Haar measure on

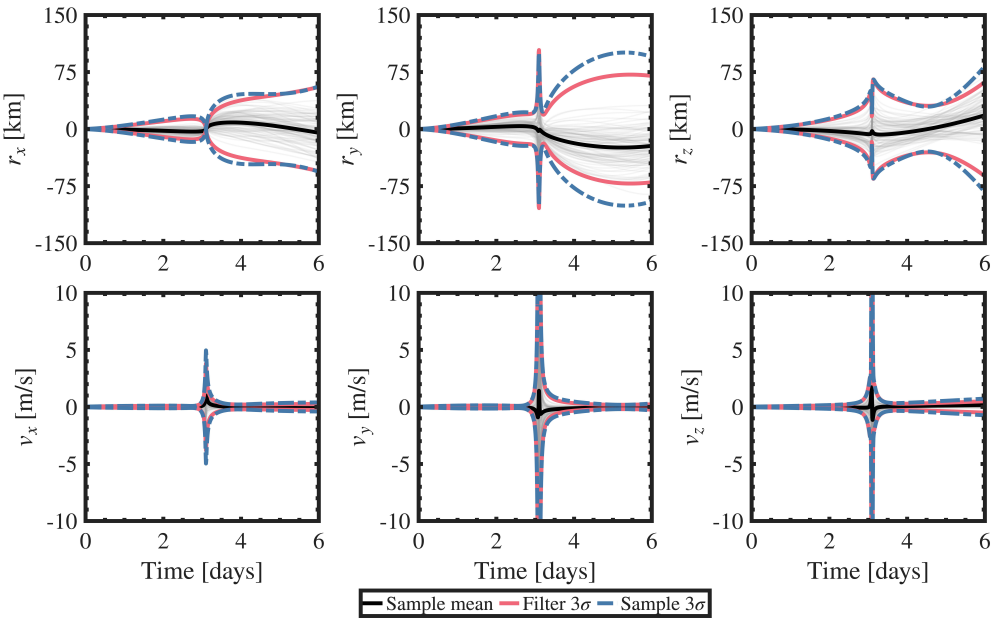


Fig. 11 Estimation error as a function of time for the attitude error modeled as Gaussian noise and using a first-order approximation in the filter. The gray lines show the estimation error for each MC. The solid black shows the sample error mean. The red solid line shows the estimated error variance, and the dashed blue line shows the mean square of the estimation error.

the rotation group $SO(3)$. The Haar measure is the unique, up to a scaling constant, measure on $SO(3)$ that is invariant under group multiplication. When normalized to have unit total measure, it defines the uniform probability distribution over rotations. The corresponding distribution of a unit vector obtained by applying a uniformly distributed rotation is rotationally invariant and hence uniform over the unit sphere. For completeness, the Haar theorem underlying this result is stated below.

Theorem 1 (Haar Measure on $SO(3)$) *There exists a unique probability measure μ on $SO(3)$, called the* normalized Haar measure, *that is invariant under left multiplication. That is, for every measurable set $\mathcal{A} \subseteq SO(3)$ and every fixed rotation $\boldsymbol{Q} \in SO(3)$,*

$$\mu(\boldsymbol{Q}\mathcal{A}) = \mu(\mathcal{A}). \tag{81}$$

Equivalently, for every integrable function $f : SO(3) \to \mathbb{R}$,

$$\int_{SO(3)} f(\boldsymbol{T})\, d\mu(\boldsymbol{T}) = \int_{SO(3)} f(\boldsymbol{Q}\boldsymbol{T})\, d\mu(\boldsymbol{T}). \tag{82}$$

Since $SO(3)$ is compact, the normalized Haar measure is also invariant under right multiplication.

Proof A proof of the existence and uniqueness of the Haar measure on locally compact groups, together with its invariance properties, can be found in [16]. □

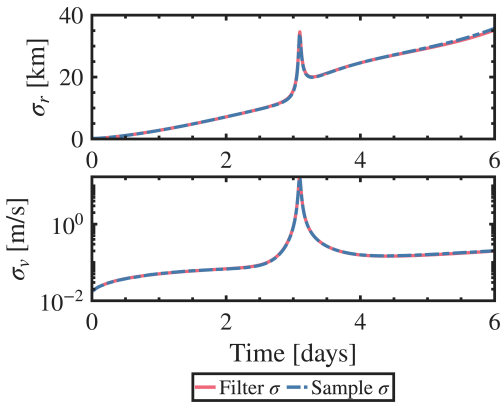


Fig. 12 Standard deviation profiles as a function of time for the attitude error modeled as Gaussian noise and using a second-order approximation in the filter. The red solid line shows the sample standard deviation. The blue dashed line shows the predicted standard deviation.

The rotational invariance of the uniform vent-direction distribution can be used to evaluate its first and second moments. In particular, the mean vent direction is given by

$$\boldsymbol{d}_k = \mathbb{E}\big[\boldsymbol{u}^I_{v,k}\big]\,. \tag{83}$$

Since the distribution of $\boldsymbol{u}^I_{v,k}$ is invariant under left multiplication by any fixed rotation $\boldsymbol{Q} \in SO(3)$,

$$\mathbb{E}\big[\boldsymbol{u}^I_{v,k}\big] = \boldsymbol{Q}\,\mathbb{E}\big[\boldsymbol{u}^I_{v,k}\big]\,, \qquad \forall\, \boldsymbol{Q} \in SO(3). \tag{84}$$

The only vector invariant under every rotation is the zero vector. Therefore, the mean vent direction is

$$\boldsymbol{d}_k = \boldsymbol{0}. \tag{85}$$

The second moment is given by

$$\boldsymbol{D}_k = \mathbb{E}\Big[\boldsymbol{u}^I_{v,k}{\boldsymbol{u}^I_{v,k}}^T\Big] = \mathbb{E}\Big[\boldsymbol{T}^I_{B,k}\boldsymbol{u}^B_v\,\big(\boldsymbol{u}^B_v\big)^T\,\Big(\boldsymbol{T}^I_{B,k}\Big)^T\Big]\,. \tag{86}$$

Applying the same invariance argument, for any $\boldsymbol{Q} \in SO(3)$,

$$\boldsymbol{D}_k = \boldsymbol{Q}\,\boldsymbol{D}_k\,\boldsymbol{Q}^T. \tag{87}$$

The only second-order tensor invariant under every rotation is a scalar multiple of the identity. Therefore,

$$\boldsymbol{D}_k = c\,\boldsymbol{I}_3, \tag{88}$$

where the constant c is determined by taking the trace,

$$3c = \mathrm{tr}(\boldsymbol{D}_k) = \mathbb{E}\Big[\mathrm{tr}\Big(\boldsymbol{u}^I_{v,k}{\boldsymbol{u}^I_{v,k}}^T\Big)\Big] = \mathbb{E}\big[\|\boldsymbol{u}^I_{v,k}\|^2\big] = 1, \tag{89}$$

which gives

$$\boldsymbol{D}_k = \frac{1}{3}\boldsymbol{I}_3. \tag{90}$$

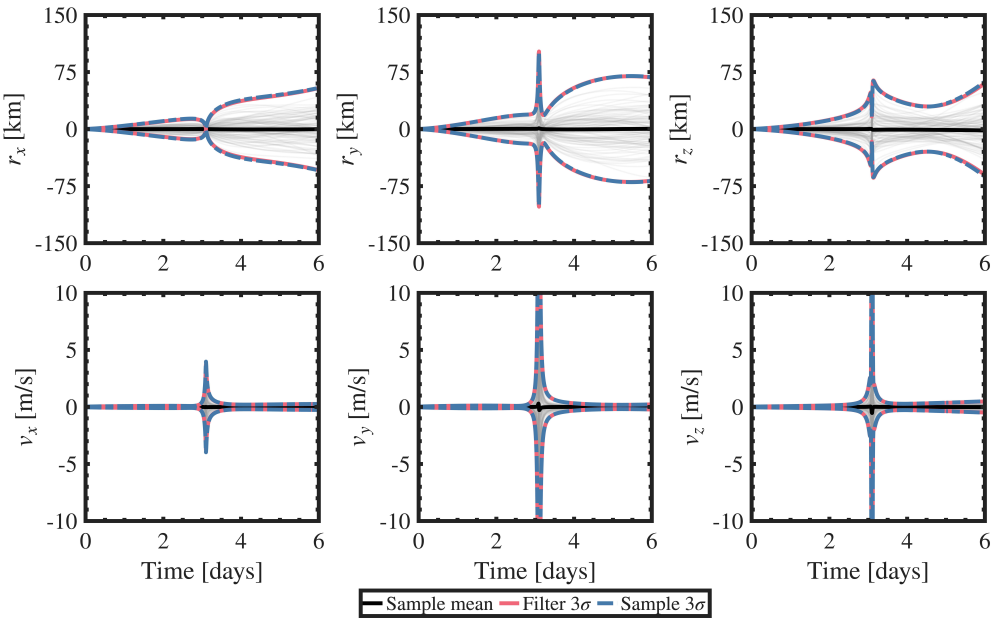


Fig. 13 Estimation error as a function of time for the attitude error modeled as Gaussian noise and using a second-order approximation in the filter. The gray lines show the estimation error for each MC. The solid black shows the sample error mean. The red solid line shows the estimated error variance, and the dashed blue line shows the mean square of the estimation error.

More generally, the same argument applies to a unit vector uniformly distributed on the p-dimensional unit sphere in $\mathbb{R}^p$, for which the second-order moment is given by $p^{-1}\boldsymbol{I}_p$ [17].

These expressions provide the exact first two moments of the vent direction under uniformly distributed attitude uncertainty. The results of the MC simulation are shown in figs. 14 and 15. In particular, fig. 14 shows that the filter-predicted standard deviation agrees well with the sample standard deviation over most of the simulation. During the final portion of the trajectory, however, the filter becomes slightly optimistic in the position estimate. This behavior is likely attributable to the relatively high level of uncertainty in this case compared with the other simulations. As the uncertainty increases, the position error may extend beyond the region in which the linearization provides an accurate approximation of the nonlinear dynamics. Consequently, neglecting higher-order terms in the covariance propagation may result in an underestimation of the true estimation uncertainty. The same behavior is reflected in fig. 15. The estimation errors remain approximately unbiased, and the predicted covariance agrees well with the sample covariance over most of the trajectory. The main exception is the r_x component during the final portion of the simulation, for which the filter slightly underestimates the uncertainty.

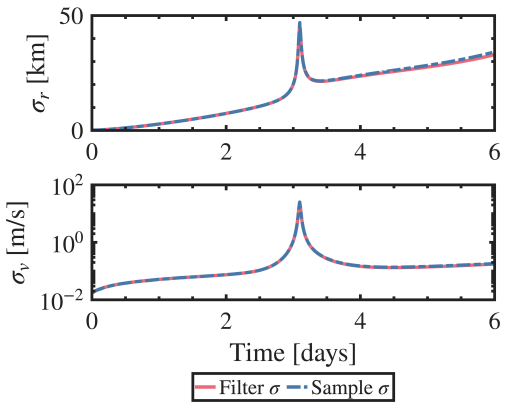


Fig. 14 Standard deviation profiles as a function of time for the vent direction uniformly distributed. The red solid line shows the sample standard deviation. The blue dashed line shows the predicted standard deviation.

5.7 Attitude Error as a Gauss–Markov Process

As a final numerical example, the attitude error is modeled as a first-order Gauss–Markov process [18]. Similar to the Gaussian attitude uncertainty considered in section 5.5, the spacecraft attitude is represented by a direction cosine matrix, while the attitude error is parameterized locally by a small rotation vector $\delta\boldsymbol{\alpha}$,

$$\boldsymbol{u}_{v,k}^{I} = \exp\left(-\left[\delta\boldsymbol{\alpha}_k\right]_\times\right) \bar{\boldsymbol{T}}_{B,k}^{I}\, \boldsymbol{u}_{v}^{B}, \tag{91}$$

where $\bar{\boldsymbol{T}}_{B}^{I}$ denotes the nominal attitude. Unlike the previous example, the attitude error is no longer assumed to be an independent Gaussian random variable at each time step. Instead, it evolves according to a first-order Gauss–Markov process, introducing temporal correlation into the attitude uncertainty. In discrete time, the process is described by

$$\delta\boldsymbol{\alpha}_{k+1} = \exp\left(-\frac{\Delta t_k}{\tau}\right) \delta\boldsymbol{\alpha}_k + \boldsymbol{\omega}_k, \tag{92}$$

where τ is the process time constant and

$$\boldsymbol{\omega}_k \sim \mathcal{N}\left(\mathbf{0},\, \boldsymbol{\Sigma}_a \left[1 - \exp\left(-\frac{2\Delta t_k}{\tau}\right)\right]\right), \tag{93}$$

with $\boldsymbol{\Sigma}_a$ denoting the steady-state covariance of the process.

Since the attitude error is modeled as a time correlated stochastic process, it cannot be represented as independent process noise acting on the translational dynamics. The resulting acceleration uncertainty is likewise correlated in time, violating the white-noise assumption commonly adopted for process disturbances. The navigation filter is therefore augmented to estimate the attitude error together with the original navigation states. In this way, the time correlated process is explicitly modeled as part of the system state, yielding an equivalent first-order Markov process that can

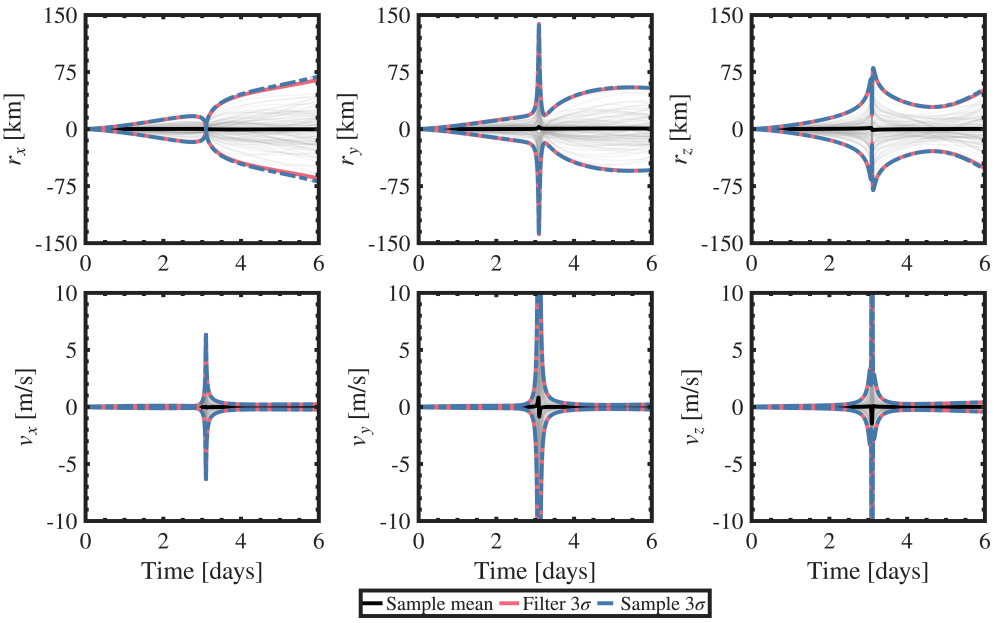


Fig. 15 Estimation error as a function of time for the vent direction uniformly distributed. The gray lines show the estimation error for each MC. The solid black shows the sample error mean. The red solid line shows the estimated error variance, and the dashed blue line shows the mean square of the estimation error.

be handled within the Kalman filtering framework. Accordingly, the augmented state vector is defined as

$$\boldsymbol{x}_k^{\text{aug}} = \begin{bmatrix} \boldsymbol{r}_k \\ \boldsymbol{v}_k \\ \delta\boldsymbol{\alpha}_k \end{bmatrix}. \tag{94}$$

It is straightforward to show that the framework developed in section 4 remains applicable after augmenting the state with the attitude error. The only modification is the process noise covariance, which becomes

$$\boldsymbol{Q}_k^{\text{aug}} = \begin{bmatrix} \boldsymbol{Q}_k & \boldsymbol{0}_{6\times 3} \\ \boldsymbol{0}_{3\times 6} & \boldsymbol{\Sigma}_a \left[1 - \exp\left(-\frac{2\Delta t_k}{\tau}\right)\right] \end{bmatrix}, \tag{95}$$

where $\boldsymbol{Q}_k$ is defined in eqs. (54) to (56).

As in the previous examples, the proposed method requires the first two moments of the vent direction. Let $\delta\bar{\boldsymbol{\alpha}}_k$ and $\boldsymbol{P}_k^{\alpha\alpha}$ denote the mean and covariance of the attitude error estimated by the filter at time t_k. Following the approach of section 5.5, a second-order Taylor series approximation is employed to evaluate the mean vent direction,

$$\boldsymbol{d}_k \approx \left(\boldsymbol{I}_3 - [\delta\bar{\boldsymbol{\alpha}}_k]_\times + \frac{1}{2}\left(\boldsymbol{P}_k^{\alpha\alpha} + \delta\bar{\boldsymbol{\alpha}}_k\delta\bar{\boldsymbol{\alpha}}_k^T\right) - \frac{1}{2}\left(\text{tr}\left(\boldsymbol{P}_k^{\alpha\alpha} + \|\delta\bar{\boldsymbol{\alpha}}_k\|^2\right)\boldsymbol{I}_3\right)\right)\bar{\boldsymbol{T}}_{B,k}^I\,\boldsymbol{u}_v^B. \tag{96}$$

while a first-order approximation is used to compute its covariance,

$$\boldsymbol{D}_k \approx \left[\bar{\boldsymbol{T}}^I_{B,k}\boldsymbol{u}^B_v\right]_\times \boldsymbol{P}^{\alpha\alpha}_k \left[\bar{\boldsymbol{T}}^I_{B,k}\boldsymbol{u}^B_v\right]^T_\times . \tag{97}$$

For this numerical example, the attitude error is modeled using a time constant of $\tau = 10\,\mathrm{s}$ and a conservative steady-state covariance $\boldsymbol{\Sigma}_a = (8\,\mathrm{deg})^2\boldsymbol{I}_3$. Figures 16 and 17 shows the resulting position and velocity estimation errors. Overall, the filter remains consistent throughout the simulation, with the estimation error remaining centered around zero and the predicted covariance closely matching the empirical covariance obtained from the MC runs.

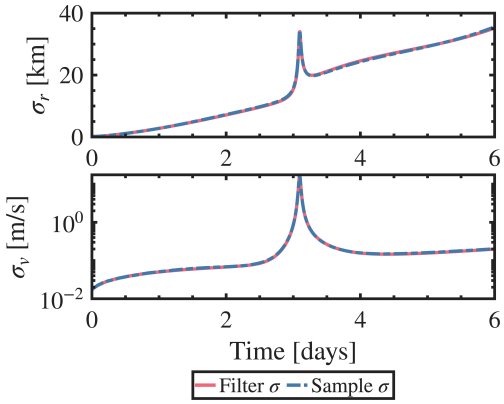


Fig. 16 Standard deviation profiles as a function of time for the attitude error modeled as a first-order Gauss–Markov process. The red solid line shows the sample standard deviation. The blue dashed line shows the predicted standard deviation.

6 Conclusions

This paper presented a new approach for modeling venting perturbations in crewed space missions. Venting events were modeled as a Gaussian–Poisson point process, where the number of vents followed a Poisson distribution, the vent magnitudes were Gaussian distributed, and the vent directions could be uncertain. Based on this model, an analytical expression for the process noise covariance was derived.

An accurate representation of venting perturbations was important for spacecraft navigation because individual venting events were generally too small to be directly detected by onboard sensors and could occur in directions that made them difficult to observe from ground-based measurements. The proposed analytical covariance therefore provided a means of accounting for the effects of venting in navigation filters without relying on ad hoc manual covariance tuning.

The proposed model was evaluated through a series of numerical examples in a filtering scenario. In all cases, the spacecraft was assumed to orbit a southern 9:2 near-rectilinear halo orbit (NRHO), and an extended Kalman filter (EKF) was used

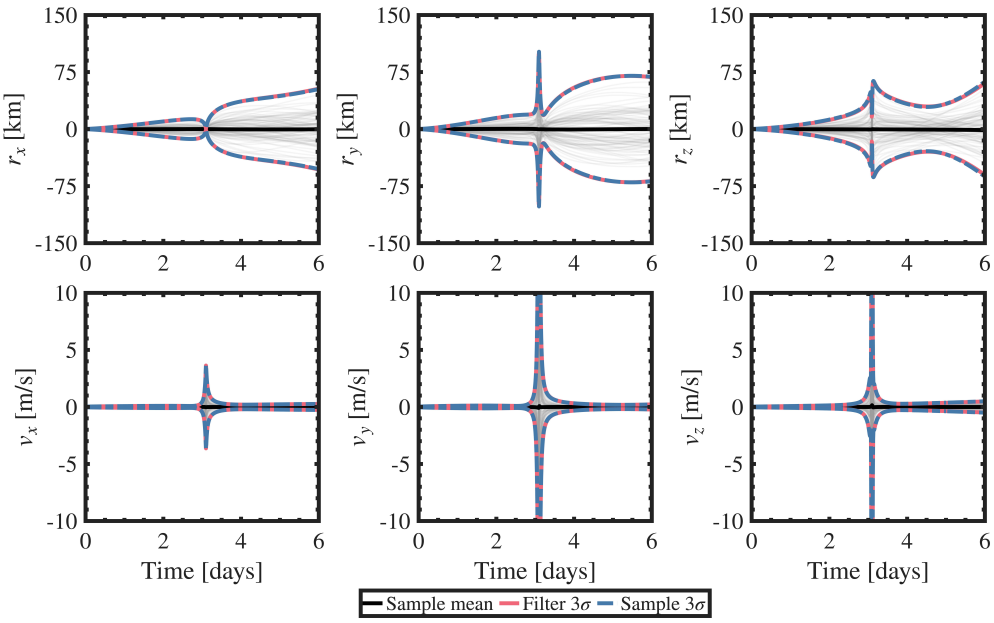


Fig. 17 Estimation error as a function of time for the attitude error modeled as a first-order Gauss–Markov process. The gray lines show the estimation error for each MC. The solid black shows the sample error mean. The red solid line shows the estimated error variance, and the dashed blue line shows the mean square of the estimation error.

to estimate the spacecraft position and velocity. In the first three examples, the vent direction was assumed to be known. The first example considered instantaneous venting events in both the truth model and the filter model, and the resulting covariance closely agreed with the Monte Carlo (MC) results. The second and third examples introduced a mismatch between the filter and truth models by modeling the true vents as finite-duration perturbations. Despite this mismatch, the proposed Gaussian–Poisson process model produced covariance estimates that closely agreed with the MC results, even when only one measurement update was performed per day.

The fourth through sixth examples investigated uncertainty in the vent direction. These results demonstrated that directional uncertainty could be incorporated into the proposed framework and that accurate covariance estimates could be obtained provided that the effects of linearization were appropriately considered. In particular, the results highlighted that increasing directional uncertainty could lead to larger state uncertainties, potentially reducing the validity of the linearized covariance propagation.

Overall, the results demonstrated that the proposed model provided an informed and practical approach for incorporating venting perturbations into spacecraft navigation filters. Although the model represented venting events as instantaneous point processes, the numerical results indicated that it could also provide an accurate representation of the resulting uncertainty when the actual vents occurred over a

finite duration. The proposed formulation therefore provided a systematic alternative to empirical covariance tuning for accounting for venting disturbances in crewed spacecraft navigation.

Appendix A Relation to Conventional Filter-Tuning Models

In this appendix, the framework derived in section 4 is applied to two filter-tuning strategies for modeling venting perturbations. In the first approach, venting is represented directly as process noise, and the proposed framework is used to determine the corresponding process noise magnitude. In the second approach, the venting acceleration is modeled as a first-order Gauss–Markov process, and the framework is instead used to determine the parameters of the process model. Both approaches consider the case in which the vent direction in the reference frame is known and characterized by its mean $\boldsymbol{d}_k$, with zero directional covariance, $\boldsymbol{D}_k = \boldsymbol{0}$. The two approaches are presented in turn, followed by a numerical analysis comparing their performance with that of the proposed venting model.

Before proceeding, an overview of the fourth-order Runge–Kutta integrator used throughout this appendix is given [13]. Consider a system governed by

$$\dot{\boldsymbol{z}}(t) = \boldsymbol{f}(t, \boldsymbol{z}(t)), \tag{A1}$$

with initial condition $\boldsymbol{z}(t_0) = \boldsymbol{z}_0$. The integrator advances the solution from t_0 to $t_1 = t_0 + \Delta t$ according to

$$\boldsymbol{z}(t_1) = \boldsymbol{z}_0 + \frac{\Delta t}{6}\left(\boldsymbol{k}_0 + 2\boldsymbol{k}_1 + 2\boldsymbol{k}_2 + \boldsymbol{k}_3\right), \tag{A2}$$

where $\boldsymbol{k}_0$, $\boldsymbol{k}_1$, $\boldsymbol{k}_2$, and $\boldsymbol{k}_3$ are given by

$$\boldsymbol{k}_0 = \boldsymbol{f}(t_0, \boldsymbol{z}_0), \tag{A3}$$

$$\boldsymbol{k}_1 = \boldsymbol{f}\left(t_0 + \frac{1}{2}\Delta t, \boldsymbol{z}_0 + \frac{1}{2}\Delta t\, \boldsymbol{k}_0\right), \tag{A4}$$

$$\boldsymbol{k}_2 = \boldsymbol{f}\left(t_0 + \frac{1}{2}\Delta t, \boldsymbol{z}_0 + \frac{1}{2}\Delta t\, \boldsymbol{k}_1\right), \tag{A5}$$

$$\boldsymbol{k}_3 = \boldsymbol{f}(t_0 + \Delta t, \boldsymbol{z}_0 + \Delta t\, \boldsymbol{k}_2). \tag{A6}$$

A.1 Venting as Process Noise

In this section, the vent acceleration is modeled as white process noise. Considering the linearization around the best estimates introduced in section 4, the variational equations governing the effect of the vent-acceleration process noise are

$$\delta\dot{\boldsymbol{r}}(t) = \delta\boldsymbol{v}(t), \tag{A7}$$

$$\delta\dot{\boldsymbol{v}}(t) = \boldsymbol{G}(\hat{\boldsymbol{r}}(t))\delta\boldsymbol{r} + \boldsymbol{d}(t)\, w_v(t), \tag{A8}$$

where $\boldsymbol{d}(t)$ is the unit vent direction at time t and $w_v(t)$ is the vent acceleration magnitude (in units of $\mathrm{m/s^2}$ or $\mathrm{ft/s^2}$), modeled as a zero-mean disturbance with statistics

$$\mathbb{E}[w_v(t)] = 0, \qquad \mathbb{E}[w_v(t)\, w_v(\tau)] = Q_v\, \delta(t-\tau), \tag{A9}$$

where Q_v is the power spectral density (of units $\mathrm{m^2/s^3}$ or $\mathrm{ft^2/s^3}$) of the vent-acceleration process noise, and δ is the Dirac delta function.

With $\boldsymbol{A}(t)$ and $\boldsymbol{B}(t)$ defined as

$$\boldsymbol{A}(t) = \begin{bmatrix} \boldsymbol{0}_{3\times3} & \boldsymbol{I}_3 \\ \boldsymbol{G}(\hat{\boldsymbol{r}}(t)) & \boldsymbol{0}_{3\times3} \end{bmatrix}, \quad \boldsymbol{B}(t) = \begin{bmatrix} \boldsymbol{0}_{3\times1} \\ \boldsymbol{d}(t) \end{bmatrix}, \tag{A10}$$

the process noise covariance matrix, $\boldsymbol{Q}_{\mathrm{PN}}(t)$ (from $\dot{\boldsymbol{P}}(t) = \boldsymbol{A}(t)\boldsymbol{P}(t) + \boldsymbol{P}(t)\boldsymbol{A}(t)^T + \boldsymbol{Q}_{\mathrm{PN}}(t)$), is the solution of the following differential equation

$$\begin{cases} \dot{\boldsymbol{Q}}_{\mathrm{PN}}(t) = \boldsymbol{A}(t)\boldsymbol{Q}_{\mathrm{PN}}(t) + \boldsymbol{Q}_{\mathrm{PN}}(t)\boldsymbol{A}(t)^T + \boldsymbol{B}(t)Q_v\boldsymbol{B}^T(t), \\ \boldsymbol{Q}_{\mathrm{PN}}(t_0) = \boldsymbol{0}_{6\times6}. \end{cases} \tag{A11}$$

Using a fourth-order Runge–Kutta method, the solution can be found, partitioned as follows

$$\boldsymbol{Q}_{\mathrm{PN}}(t) = \begin{bmatrix} \boldsymbol{Q}_{\mathrm{PN}}^{(1:3,1:3)}(t) & \boldsymbol{Q}_{\mathrm{PN}}^{(1:3,4:6)}(t) \\ \boldsymbol{Q}_{\mathrm{PN}}^{(4:6,1:3)}(t) & \boldsymbol{Q}_{\mathrm{PN}}^{(4:6,4:6)}(t) \end{bmatrix}, \tag{A12}$$

where

$$\boldsymbol{Q}_{\mathrm{PN}}^{(1:3,1:3)}(t) = \frac{Q_v}{3}\Delta t^3 \boldsymbol{d}_k \boldsymbol{d}_k^T, \tag{A13}$$

$$\boldsymbol{Q}_{\mathrm{PN}}^{(1:3,4:6)}(t) = \frac{Q_v}{2}\Delta t^2 \boldsymbol{d}_k \boldsymbol{d}_k^T + \frac{Q_v}{8}\Delta t^4 \boldsymbol{d}_k \boldsymbol{d}_k^T \boldsymbol{G}_k^T + \frac{Q_v}{24}\Delta t^4 \boldsymbol{G}_k \boldsymbol{d}_k \boldsymbol{d}_k^T, \tag{A14}$$

$$\boldsymbol{Q}_{\mathrm{PN}}^{(4:6,4:6)}(t) = Q_v \Delta t \boldsymbol{d}_k \boldsymbol{d}_k^T + \frac{Q_v}{6}\Delta t^3 \left(\boldsymbol{G}_k \boldsymbol{d}_k \boldsymbol{d}_k^T + \boldsymbol{d}_k \boldsymbol{d}_k^T \boldsymbol{G}_k^T \right). \tag{A15}$$

Comparing eqs. (54) to (56) with eqs. (A13) to (A15), there are strong correspondences between the Gaussian–Poisson vent model and the process noise vent model. Specifically

$$Q_v \mathrel{\widehat{=}} \lambda(\mu_v^2 + \sigma_v^2), \tag{A16}$$

where λ is the mean (arrival) time (in units of 1/Time) of the vent impulses, μ_v is the mean vent impulse (in units of Length/Time), σ_v^2 is the variance of the vent impulse (in units of $\mathrm{Length^2/Time^2}$), and Q_v is the corresponding process noise due to the vent acceleration (expressed as a power spectral density in units of $\mathrm{Length^2/Time^3}$).

A.2 Venting as a First-Order Gauss–Markov Process

In this section, the vent acceleration is modeled as a first-order Gauss–Markov process. Considering the linearization around the best estimates introduced in section 4, the

corresponding variational equations are

$$\delta\dot{\boldsymbol{r}}(t) = \delta\boldsymbol{v}(t), \tag{A17}$$
$$\delta\dot{\boldsymbol{v}}(t) = \boldsymbol{G}(\hat{\boldsymbol{r}}(t))\delta\boldsymbol{r} + \boldsymbol{d}(t)\, a_v(t), \tag{A18}$$
$$\dot{a}_v(t) = -\frac{1}{\tau_v} a_v(t) + w_a(t), \tag{A19}$$

where a_v is the vent acceleration magnitude (in units of Length/Time^2), modeled as a first-order Gauss–Markov process driven by the zero-mean white noise $w_a(t)$, with statistics

$$\mathbb{E}[w_a(t)] = 0 \qquad \mathbb{E}[w_a(t)\, w_a(\tau)] = Q_a\, \delta(t-\tau), \tag{A20}$$

where Q_v is the power spectral density (of units Length^2/Time^5) of the white noise driving the Gauss–Markov process, and δ is the Dirac delta function.

Defining the augmented state vector $\delta\boldsymbol{x}$ and the matrices $\boldsymbol{A}(t)$ and $\boldsymbol{B}(t)$ as

$$\delta\boldsymbol{x} = \begin{bmatrix} \delta\boldsymbol{r} \\ \delta\boldsymbol{v} \\ a_v \end{bmatrix}, \qquad \boldsymbol{A}(t) = \begin{bmatrix} \boldsymbol{0}_{3\times3} & \boldsymbol{I}_3 & \boldsymbol{0}_{3\times1} \\ \boldsymbol{G}(\hat{\boldsymbol{r}}(t)) & \boldsymbol{0}_{3\times3} & \boldsymbol{d}(t) \\ \boldsymbol{0}_{1\times3} & \boldsymbol{0}_{1\times3} & -\dfrac{1}{\tau_v} \end{bmatrix}, \quad \boldsymbol{B}(t) = \begin{bmatrix} \boldsymbol{0}_{3\times1} \\ \boldsymbol{0}_{3\times1} \\ 1 \end{bmatrix}, \tag{A21}$$

the variational equations above can be written in the compact form

$$\delta\dot{\boldsymbol{x}}(t) = \boldsymbol{A}(t)\, \delta\boldsymbol{x}(t) + \boldsymbol{B}(t)\, w_a(t). \tag{A22}$$

For this system, the solution of the covariance propagation equation is

$$\boldsymbol{P}(t) = \boldsymbol{\Phi}(t, t_0)\boldsymbol{P}(t_0)\boldsymbol{\Phi}^T(t, t_0) + \overline{\boldsymbol{Q}}(t), \tag{A23}$$

where $\boldsymbol{\Phi}(t, t_0)$ is the state transition matrix associated with $\boldsymbol{A}(t)$, and $\overline{\boldsymbol{Q}}$ is the solution of

$$\begin{cases} \dot{\overline{\boldsymbol{Q}}}(t) = \boldsymbol{A}(t)\overline{\boldsymbol{Q}}(t) + \overline{\boldsymbol{Q}}(t)\boldsymbol{A}(t)^T + \boldsymbol{B}(t)Q_v\boldsymbol{B}^T(t), \\ \overline{\boldsymbol{Q}}(t_0) = \boldsymbol{0}_{7\times7}. \end{cases} \tag{A24}$$

Using a fourth-order Runge–Kutta integrator, the solution of eq. (A24) is

$$\overline{\boldsymbol{Q}}(t) = \begin{bmatrix} \overline{\boldsymbol{Q}}^{rr}(t) & \overline{\boldsymbol{Q}}^{rv}(t) & \overline{\boldsymbol{Q}}^{ra}(t) \\ (\overline{\boldsymbol{Q}}^{rv}(t))^T & \overline{\boldsymbol{Q}}^{vv}(t) & \overline{\boldsymbol{Q}}^{va}(t) \\ (\overline{\boldsymbol{Q}}^{ra}(t))^T & (\overline{\boldsymbol{Q}}^{va}(t))^T & \overline{\boldsymbol{Q}}^{aa}(t) \end{bmatrix}, \tag{A25}$$

where

$$\overline{\boldsymbol{Q}}^{rr}(t) = \boldsymbol{0}_{3\times3}, \tag{A26}$$

$$\overline{\boldsymbol{Q}}^{rv}(t) = \frac{\Delta t^4 Q_a}{8}\boldsymbol{d}_k\boldsymbol{d}_k^T, \tag{A27}$$

$$\overline{\boldsymbol{Q}}^{vv}(t) = \frac{\Delta t^3 Q_a}{12}\left(4 - \frac{3\Delta t}{\tau_a}\right)\boldsymbol{d}_k\boldsymbol{d}_k^T, \tag{A28}$$

$$\overline{\boldsymbol{Q}}^{ra}(t) = \frac{\Delta t^3 Q_a}{6}\left(1 - \frac{\Delta t}{\tau_a}\right)\boldsymbol{d}_k, \tag{A29}$$

$$\overline{\boldsymbol{Q}}^{va}(t) = \frac{\Delta t^2 Q_a}{6}\left(3 - \frac{3\Delta t}{\tau_a} + \frac{7\Delta t^2}{4\tau_a^2} + \frac{\Delta t^2}{4}\boldsymbol{G}_k\right)\boldsymbol{d}_k, \tag{A30}$$

$$\overline{\boldsymbol{Q}}^{aa}(t) = \frac{\tau_a Q_a}{2}\left(1 - e^{-\frac{2\Delta t}{\tau_a}}\right). \tag{A31}$$

Consider the state partitioned into the standard position-and-velocity state, $\delta\boldsymbol{s}(t) = \begin{bmatrix}\delta\boldsymbol{r}^T(t) & \delta\boldsymbol{v}^T(t)\end{bmatrix}^T$, and the acceleration state $a_v(t)$, so that $\delta\boldsymbol{x} = \begin{bmatrix}\delta\boldsymbol{s}^T & a_v\end{bmatrix}^T$ and the covariance $\boldsymbol{P}(t)$ and state transition matrix $\boldsymbol{\Phi}(t, t_0)$ are partitioned accordingly as

$$\boldsymbol{P}(t) = \begin{bmatrix}\boldsymbol{P}_{ss}(t) & \boldsymbol{P}_{sa}(t)\\ \boldsymbol{P}_{sa}^T(t) & P_{aa}(t)\end{bmatrix}, \qquad \boldsymbol{\Phi}(t, t_0) = \begin{bmatrix}\boldsymbol{\Phi}_{ss}(t, t_0) & \boldsymbol{\Phi}_{sa}(t, t_0)\\ \boldsymbol{0}_{1\times 6} & \Phi_{aa}(t, t_0)\end{bmatrix}. \tag{A32}$$

Considering $\boldsymbol{P}_{sa}(t_0) = \boldsymbol{0}_{6\times 1}$ and $P_{aa}(t_0) = \sigma_a^2$, the covariance propagation for the position-and-velocity state in eq. (A23) becomes

$$\boldsymbol{P}_{ss}(t) = \boldsymbol{\Phi}_{ss}(t, t_0)\boldsymbol{P}_{ss}(t_0)\boldsymbol{\Phi}_{ss}^T(t, t_0) + \sigma_a^2\,\boldsymbol{\Phi}_{sa}(t, t_0)\boldsymbol{\Phi}_{sa}^T(t, t_0) + \overline{\boldsymbol{Q}}_{ss}(t), \tag{A33}$$

where $\overline{\boldsymbol{Q}}_{ss}(t)$ is the corresponding block of $\overline{\boldsymbol{Q}}(t)$, assembled from $\overline{\boldsymbol{Q}}^{rr}(t)$, $\overline{\boldsymbol{Q}}^{rv}(t)$, and $\overline{\boldsymbol{Q}}^{vv}(t)$ as defined above. Therefore, it is possible to define an equivalent process noise covariance as

$$\boldsymbol{Q}_{\mathrm{GM}}(t) = \sigma_a^2\,\boldsymbol{\Phi}_{sa}(t, t_0)\boldsymbol{\Phi}_{sa}^T(t, t_0) + \overline{\boldsymbol{Q}}_{ss}(t), \tag{A34}$$

where, integrating the state transition matrix with a fourth-order Runge–Kutta integrator, yields

$$\boldsymbol{Q}_{\mathrm{GM}}^{(1:3,1:3)}(t) = \sigma_a^2\frac{\Delta t^4}{4}\boldsymbol{d}_k\boldsymbol{d}_k^T, \tag{A35}$$

$$\boldsymbol{Q}_{\mathrm{GM}}^{(1:3,4:6)}(t) = \sigma_a^2\frac{\Delta t^3}{2}\left(1 - \frac{5\Delta t}{6\tau_a}\right)\boldsymbol{d}_k\boldsymbol{d}_k^T, \tag{A36}$$

$$\begin{aligned}\boldsymbol{Q}_{\mathrm{GM}}^{(4:6,4:6)}(t) =& \sigma_a^2\Delta t^2\left(1 - \frac{\Delta t}{\tau_a} + \frac{7\Delta t^2}{12\tau_a^2}\right)\boldsymbol{d}_k\boldsymbol{d}_k^T\\ &+ \sigma_a^2\frac{\Delta t^4}{6}\left(\boldsymbol{G}_k\boldsymbol{d}_k\boldsymbol{d}_k^T + \boldsymbol{d}_k\boldsymbol{d}_k^T\boldsymbol{G}_k^T\right)\\ &+ \frac{\Delta t^3 Q_a}{12}\left(4 - \frac{3\Delta t}{\tau_a}\right)\boldsymbol{d}_k\boldsymbol{d}_k^T.\end{aligned} \tag{A37}$$

The objective now is to find values for the unknowns σ_a^2, Q_a, and τ_a such that eqs. (A35) to (A37) closely match eqs. (A13) to (A15). Equating eq. (A35) with

eq. (A13) gives

$$\sigma_a^2 = \frac{4}{3\Delta t} Q_v \quad \Longleftrightarrow \quad \frac{\sigma_a^2}{Q_v} = \frac{4}{3\Delta t}. \tag{A38}$$

Denoting

$$\boldsymbol{C} = \frac{\Delta t^3}{2} \left(\boldsymbol{G}_k \boldsymbol{d}_k \boldsymbol{d}_k^T + \boldsymbol{d}_k \boldsymbol{d}_k^T \boldsymbol{G}_k^T \right), \tag{A39}$$

equating eq. (A36) with eq. (A14) and substituting eq. (A38) gives

$$\boldsymbol{C} = \Delta t \left[\frac{2}{3} \left(1 - \frac{10\Delta t}{3\tau_a} \right) + \frac{\Delta t^2 Q_a}{2 Q_v} \right] \boldsymbol{d}_k \boldsymbol{d}_k^T. \tag{A40}$$

This follows the spirit of the method of *variation of parameters*, where $\boldsymbol{C}$ is now expressed in terms of the quantities of interest. Equating eq. (A37) with eq. (A15) and substituting eq. (A40) gives

$$\begin{aligned} &\sigma_a^2 \Delta t^2 \left(1 - \frac{\Delta t}{\tau_a} + \frac{7\Delta t^2}{12\tau_a^2} \right) + \frac{\Delta t^3 Q_a}{12} \left(4 - 3\frac{\Delta t}{\tau_a} \right) \\ &-\Delta t \left(\frac{Q_v}{3} - \frac{\sigma_a^2 \Delta t}{3} \right) \left[\frac{2}{3} \left(1 - \frac{10\Delta t}{3\tau_a} \right) + \frac{\Delta t^2 Q_a}{2 Q_v} \right] = 0. \end{aligned} \tag{A41}$$

Utilizing eq. (A38) and defining $\xi = \Delta t / \tau_a$ leads to

$$\left(\frac{11}{27} - \frac{128}{81}\xi + \frac{7}{9}\xi^2 \right) + \frac{Q_a \Delta t}{Q_v} \left(\frac{7}{18} - \frac{\xi}{4} \right) = 0, \tag{A42}$$

where the unknowns are ξ and Q_a. Solving for Q_a then gives

$$Q_a = \frac{-4 Q_v \left(63\xi^2 - 128\xi + 33 \right)}{9\Delta t^2 \left(14 - 9\xi \right)}. \tag{A43}$$

For Q_a to be positive, the numerator and denominator must have opposite signs, which requires

$$Q_a > 0 \quad \Longleftrightarrow \quad \left(\frac{64 - \sqrt{2017}}{63} < \xi < \frac{14}{9} \right) \quad \text{or} \quad \left(\xi > \frac{64 + \sqrt{2017}}{63} \right), \quad \xi \neq \frac{14}{9}. \tag{A44}$$

The objective now is to select a value of ξ such that the covariance produced by the Gauss–Markov process matches that of the Gauss–Poisson process described by eqs. (54) to (56). To that end, choosing $\xi = 1/3$ gives

$$\tau_a = 3\Delta t, \tag{A45}$$

$$\sigma_a^2 = \frac{4}{3} \frac{\lambda(\mu_v^2 + \sigma_v^2)}{\Delta t}, \tag{A46}$$

$$Q_a = \frac{32}{297} \frac{\lambda(\mu_v^2 + \sigma_v^2)}{\Delta t^2}, \tag{A47}$$

and the final process noise covariance matrix is

$$\boldsymbol{Q}_{\mathrm{GM}}^{(1:3,1:3)}(t) = \frac{1}{3}\lambda(\mu_v^2 + \sigma_v^2)\Delta t^3 \boldsymbol{d}_k \boldsymbol{d}_k^T, \tag{A48}$$

$$\boldsymbol{Q}_{\mathrm{GM}}^{(1:3,4:6)}(t) = 0.4949\,\lambda(\mu_v^2 + \sigma_v^2)\Delta t^2 \boldsymbol{d}_k \boldsymbol{d}_k^T, \tag{A49}$$

$$\boldsymbol{Q}_{\mathrm{GM}}^{(4:6,4:6)}(t) = 1.0022\,\lambda(\mu_v^2 + \sigma_v^2)\Delta t\, \boldsymbol{d}_k \boldsymbol{d}_k^T + \frac{2}{9}\lambda(\mu_v^2 + \sigma_v^2)\Delta t^3 \left(\boldsymbol{G}_k \boldsymbol{d}_k \boldsymbol{d}_k^T + \boldsymbol{d}_k \boldsymbol{d}_k^T \boldsymbol{G}_k^T\right). \tag{A50}$$

This analysis serves to inform the choice of the vent stochastic acceleration in the Gauss–Markov model which represents the statistics of the vent Gauss–Poisson process which in turn corresponds well with the actual vent accelerations which inform the position and velocity uncertainties. Not surprisingly, all these parameters are dependent on Δt, the integration step size.

A.3 Numerical Analysis

As a numerical check, we perform a numerical analysis following the first example presented section 5.2. For this numerical example, three filters are considered. The state propagation is identical for all three filters. The only difference among them is the process-noise covariance used in propagating the state covariance. The three covariances derived in section 4 and in this appendix are tested, namely $\boldsymbol{Q}_{\mathrm{GP}}$ defined in eqs. (54) to (56), $\boldsymbol{Q}_{\mathrm{PN}}$ defined in eqs. (A13) to (A15), and $\boldsymbol{Q}_{\mathrm{GM}}$ defined in eqs. (A35) to (A37).

To evaluate the performance of the three filters, two metrics are used: the root mean square error (RMSE) and scaled normalized estimation error squared (SNEES), defined as

$$\mathrm{RMSE}_k = \sqrt{\frac{1}{n_s}\sum_{i=1}^{n_s}\left(\boldsymbol{x}_k^{(i)} - \hat{\boldsymbol{x}}_k^{(i)}\right)^2}, \tag{A51}$$

$$\mathrm{SNEES}_k = (\boldsymbol{x}_k - \hat{\boldsymbol{x}}_k)^T \boldsymbol{P}_k^{-1}(\boldsymbol{x}_k - \hat{\boldsymbol{x}}_k), \tag{A52}$$

where $\boldsymbol{x}_k$ is the true state at time step k, $\hat{\boldsymbol{x}}_k$ is the estimated state, and $\boldsymbol{P}_k$ is the state error covariance at that time step. The number of states, n_s, is equal to 3, as the RMSE is computed separately for the position and velocity components. Note that, for a filter to be statistically consistent, the SNEES should be 1. A SNEES greater than 1 indicates an overconfident filter, whereas a SNEES less than 1 indicates a conservative filter [18].

Therefore, 1000 MC trajectories are simulated, and the MC mean RMSE (averaged over time and MC) and the MC median SNEES (first taking the median over MC for each time-step and then averaging over time) are compared for the three filters.[1] Table A1 shows the results obtained from the MC analysis. For this case, the error and covariance histories are not reported, as the results from the three filters are visually indistinguishable. As can be seen, both the position and velocity RMSE are identical

[1] The median is used for the SNEES because inverting $\boldsymbol{P}_k$ can introduce numerical issues that result in outliers.

for the three filters, as expected. The SNEES values indicate that all three filters perform equivalently and are statistically consistent. Hence, the higher-order terms in $\boldsymbol{Q}_{\mathrm{GP}}$ contribute very little, at least in this example. Overall, these results validate the three process noise covariances obtained using the different methodologies.

Table A1 Performance metrics for the three filters.

Metric	$\boldsymbol{Q}_{\mathbf{GP}}$	$\boldsymbol{Q}_{\mathbf{PN}}$	$\boldsymbol{Q}_{\mathbf{GM}}$
RMSE Position [km]	8.3283	8.3283	8.3283
RMSE Velocity [m/s]	0.13557	0.13557	0.13557
SNEES [-]	0.93105	0.93105	0.92944

References

[1] Frank H. Samonski, J., Tucker, E.M.: Apollo experience report - command and service module environmental control system. Technical report, National Aeronautics and Space Administration (1972)

[2] Apollo 8 mission report. Technical report, National Aeronautics and Space Administration (1969)

[3] Apollo 13 mission report. Technical report, National Aeronautics and Space Administration (1970)

[4] Joshi, J., D'Souza, C.: Modeling venting disturbances within linear covariance toolset for crewed artemis missions. In: AAS/AIAA Astrodynamics Specialist Conference (2023)

[5] Joshi, J.A., Gualdoni, M.J., D'Souza, C.N., Woffinden, D.C., McCabe, J.S., York, C.: Artemis ii: Linear covariance analysis using explicit vent force states. In: AAS/AIAA Astrodynamics Specialist Conference (2024)

[6] Montenbruck, O., Gill, E.: Satellite Orbits: Models, Methods, and Applications. Springer, Berlin, Heidelberg (2000). https://doi.org/10.1007/978-3-642-58351-3

[7] Baake, M., Schlaegel, U.: The peano-baker series. Proceedings of the Steklov Institute of Mathematics **275**(1), 155–159 (2011) https://doi.org/10.1134/S0081543811080098

[8] Vallado, D.A.: Fundamentals of Astrodynamics and Applications, 5th edn. Microcosm Press, Hawthorne, CA (2022)

[9] Chen, X., Tharmarasa, R., Pelletier, M., Kirubarajan, T.: Integrated clutter estimation and target tracking using poisson point processes. IEEE Transactions on

Aerospace and Electronic Systems **48**(2), 1210–1235 (2012) https://doi.org/10.1109/TAES.2012.6178058

[10] A.M., F., D.S., S.: Survey on clutter spatial intensity estimation methods for target tracking. Journal Of Advances In Information Fusion **17**(1), 3–13 (2022)

[11] Carpenter, J.R., D'Souza, C.N.: Navigation filter best practices. Technical report (2025)

[12] Ross, S.M.: Introduction to Probability Models, 12 edn. Academic Press, London, United Kingdom (2019)

[13] Butcher, J.C.: Numerical Methods for Ordinary Differential Equations. John Wiley & Sons, Chichester, England (2016)

[14] Servadio, S., Zanetti, R.: Differential algebra-based multiple gaussian particle filter for orbit determination. Journal of Optim. Theory Appl. **101**, 459–485 (2021) https://doi.org/10.1007/s10957-021-01934-8

[15] Barfoot, T.D.: State Estimation for Robotics. Cambridge University Press, Cambridge, United Kingdom (2017). https://doi.org/10.1017/9781316671528

[16] Folland, G.B.: A Course in Abstract Harmonic Analysis. CRC press, Boca Raton, FL (2016)

[17] Mardia, K.V., Jupp, P.E.: Directional Statistics. Wiley, Chichester (1999). https://doi.org/10.1002/9780470316979

[18] Bar-Shalom, Y., Li, X.R., Kirubarajan, T.: Estimation with Applications to Tracking and Navigation: Theory Algorithms and Software. John Wiley & Sons, New York, NY (2001)